Ore Geology Reviews 158 (2023) 105483

Contents lists available at ScienceDirect

Ore Geology Reviews

journal homepage: www.elsevier.com/locate/oregeorev

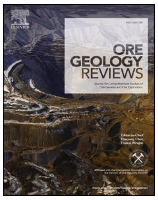

In-situ texture and geochemistry of apatite from the Jinling and Zhangjiawa iron skarn deposits, eastern North China Craton: Implications for ore-forming processes and formation of high-grade ores

Ying-Hua Chen[a,b], Ting-Guang Lan[b,*], Wei Gao[b], Lei Shu[c], Yan-Wen Tang[b], Huan-Long Hu[b]

[a] *Faculty of Land Resources Engineering, Kunming University of Science and Technology, Kunming 650093, China*
[b] *State Key Laboratory of Ore Deposit Geochemistry, Institute of Geochemistry, Chinese Academy of Sciences, Guiyang 550081, China*
[c] *MNR Key Laboratory of Gold Mineralization Processes and Resources Utilization, Shandong Institute of Geological Sciences, Jinan 250013, China*

ARTICLE INFO

Keywords:
Apatite
Halogens
Trace elements
Fluid metasomatism
Iron skarn deposit
High-grade ore

ABSTRACT

Apatite commonly contains abundant halogens and trace elements, which can occur in both the magmatic and hydrothermal stages, becoming favorable for recording the magmatic-hydrothermal properties and processes. Skarn-type iron deposits associated with high-Mg diorites are widespread in the Luxi Block, eastern North China Craton. Their ore-forming processes, especially how the different wallrocks (limestones and dolomites) controlled the formation of high-grade iron ores, have been poorly constrained. To unravel the mechanisms, in this contribution, in-situ textural, geochronological (U-Pb dating) and geochemical (halogens and trace elements) analyses by SEM, EPMA and LA-ICP-MS were conducted on apatite from the representative Fe skarn deposits (Jinling and Zhangjiawa deposits) in the Luxi Block. Three generations of apatite were identified in the Jinling deposit, which occur in the feldspathization (Ap1), garnet–pyroxene skarns (Ap2) and massive magnetite ores (Ap3), respectively. One generation of apatite occurring in the massive magnetite ores (Ap-3) was identified in the Zhangjiawa deposit. The Ap2 and Ap-3 apatite grains show patchy textures composed by residual bright zones (Ap2a and Ap-3a) and newly-formed grey to dark zones (Ap2b and Ap-3b), which indicate fluid metasomatism. LA-ICP-MS U-Pb dating shows that the Ap1, Ap2a and Ap3 apatite in the Jinling deposit formed at 130.4 ± 0.9 Ma (2σ), 128.5 ± 2.4 Ma and 128.3 ± 9.2 Ma, respectively, whereas the Ap-3a in the Zhangjiawa deposit formed at 128.1 ± 4.2 Ma. These ages are well consistent with the intrusive ages of the spatially associated high-Mg diorites within errors, corroborating the ore-forming fluids originating from the high-Mg rocks. All the studied apatite grains show F/Cl ratios higher than 1, especially in the early-stage apatite (e.g., 5–19 in Ap1), indicating that the originally exsolved fluids were enriched in F. The high F contents probably played a significant role in leaching Fe from the high-Mg rocks by enhancing rock porosities. The Eu/Eu* ratios of apatite increase from Ap2a to Ap3 while the Ce/Ce* ratios decrease. This suggests an increase of oxygen fugacity. The Sr concentrations in Ap3 are much higher than those in Ap-3a, correlating well with the wallrocks that limestones are developed in the former while dolomites in the latter. The above features indicate that fluid-rock interaction likely led to the increase of oxygen fugacity, which controlled the massive Fe deposition. In the Jinling deposit, the altered apatite grains (Ap2b) show much lower REE + Y but higher F contents than those of the unaltered (Ap2a), not only indicating the REEs being easily mobilized during metasomatism, but also suggesting that the high F contents likely contributed to the formation of high-grade ores by leaching additional Fe from the previously formed Fe-rich skarns. In the Zhangjiawa deposit, the altered apatite grains (Ap-3b) shows lower Cl contents than those of the unaltered (Ap-3a). This probably indicates the mixing of low-salinity fluids (e.g., recycling meteoric water), leading to the loss of Fe and thus lowering the Fe grade. The above results indicate that metasomatism is common in the skarn deposits, which can either elevate or lower the metal grade. The processes can be well recorded by apatite.

---

[*] Corresponding author.
E-mail address: lantingguang@126.com (T.-G. Lan).

https://doi.org/10.1016/j.oregeorev.2023.105483
Received 24 November 2022; Received in revised form 14 April 2023; Accepted 4 May 2023

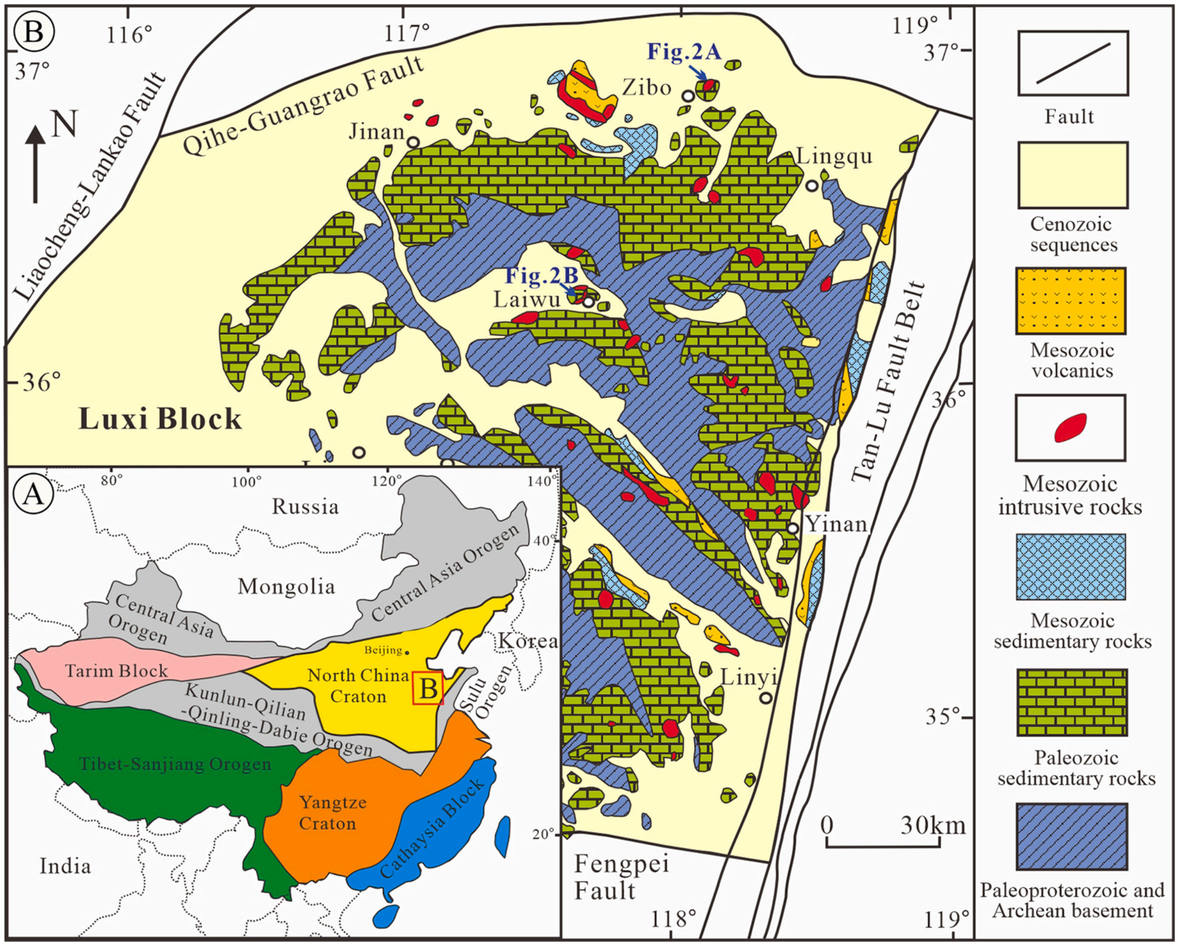

Fig. 1. Tectonic subdivision of China (A) and geological map of the Luxi block (B). (A) and (B) are modified from Mao et al. (2011) and Lan et al. (2019), respectively.

1. Introduction

Skarn deposits are the important producers of economic metals such as Fe, Cu, Pb, Zn, W and Au (Meinert et al., 2005). Taking the Fe skarn deposits for example, they account for ~ 57% of the high-grade (≥50 wt % Fe) iron resources in China (Zhang et al., 2021). Long-lasting or multistage hydrothermal fluids commonly occur in skarn deposits (e.g., Meinert et al., 1997; Chang and Meinert, 2008; Chelle-Michou et al., 2017; Li et al., 2019; Park et al., 2019), leading to the confusions of how the metals are transported and deposited. To better understand the ore-forming mechanisms, in-situ investigations on microtextures, elemental and isotopic compositions of associated minerals are necessary. Apatite can occur in both the magmatic and hydrothermal stages, which is favorable to record the entire information from the magmas to the hydrothermal fluids (Belousova et al., 2002; Cao et al., 2012; Bouzari et al., 2016; Mao et al., 2016; Roy-Garand et al., 2022). In addition, apatite commonly contains halogens (e.g., F and Cl) and abundant trace elements with multistage growth, facilitating to constrain the properties of the fluids and the specific ore-forming processes. In recent years, the geochemistry of apatite has been widely applied to study the ore-forming processes of magmatic-hydrothermal deposits, such as carbonatite-related REE deposits (Broom-Fendley et al., 2016; Chakhmouradian et al., 2017; Song et al., 2018; Andersson et al., 2019; Hu et al., 2019; Ying et al., 2020), iron-oxide apatite (IOA) deposits (Harlov et al. 2016; Zeng et al. 2016; Palma et al., 2019), and iron-oxide copper gold (IOCG) deposits (Li and Zhou, 2015; Krneta et al., 2017; Cherry et al., 2018; Xiao et al., 2021; Liao et al., 2022). Apatite is also ubiquitous in Fe skarn deposits, but has been less concerned (Zhou et al., 2022).

Numerous Fe skarn deposits associated with high-Mg diorites occurred in the Luxi Block, eastern North China Craton during the early Cretaceous (Lan et al., 2019). The Jinling and Zhangjiawa iron deposits are the two representative Fe skarn deposits in this region, accounting for about 200 and 290 million tons of iron ores with Fe grades of ~ 52% and ~ 45–50% (Jin et al., 2015; Duan and Li, 2017), respectively. The carbonatic wallrocks in the above two deposits are characterized by limestones and dolomites, respectively. The different wallrocks resulted in distinct Fe skarn ores, which have been poorly studied. In addition, because of multistage hydrothermal activities, fluid metasomatism widely occurred in the two deposits. Fluid metasomatism can significantly elevate the metal grades in REE and gold deposits (Broom-Fendley et al., 2016; Broom-Fendley et al., 2017; Hastie et al., 2020; Ying et al., 2020; Petrella et al., 2021), which might also contribute to the formation of high-grade iron ores (Hu et al., 2014). To unravel the mineralization mechanisms associated with different wallrocks (limestones and dolomites) and the effects of metasomatism on Fe grade, in this contribution, we conducted in-situ textural, geochronological (U-Pb dating) and geochemical (halogens and trace elements) analyses on apatite from different hydrothermal stages in the Jinling and Zhangjiawa Fe skarn deposits by scanning electron microscope (SEM), electron probe microanalyzer (EPMA) and laser ablation-inductively coupled plasma-mass spectrometry (LA–ICP–MS).

2. Geological setting

The North China Craton is the largest and oldest craton in China

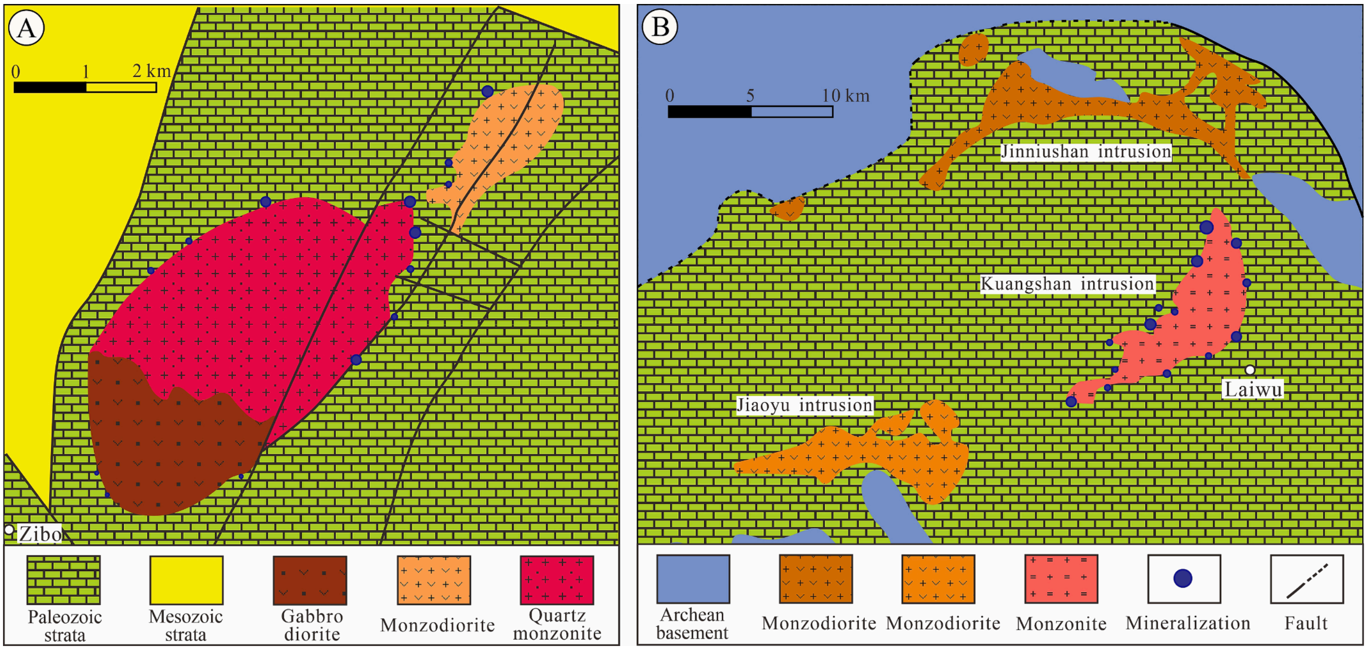

Fig. 2. Geological maps of the Jinling (A) and Zhangjiawa (B) iron deposits (modified from Lan et al., 2019).

(Fig. 1A), which is mainly constituted by a basement with Archean to Paleoproterozoic tonalitic-trondhjemitic-granodioritic (TTG) gneisses and greenschist to granulite facies volcano-sedimentary rocks and a cover with Mesoproterozoic to Neoproterozoic volcano-sedimentary rocks, Cambrian to Ordovician epicontinental carbonate rocks, Carboniferous to Permian alternating marine and terrestrial sequences and Mesozoic-Cenozoic basin sediments (Lu et al., 2008; Yang et al., 2017). It began cratonization before the Mesoproterozoic by

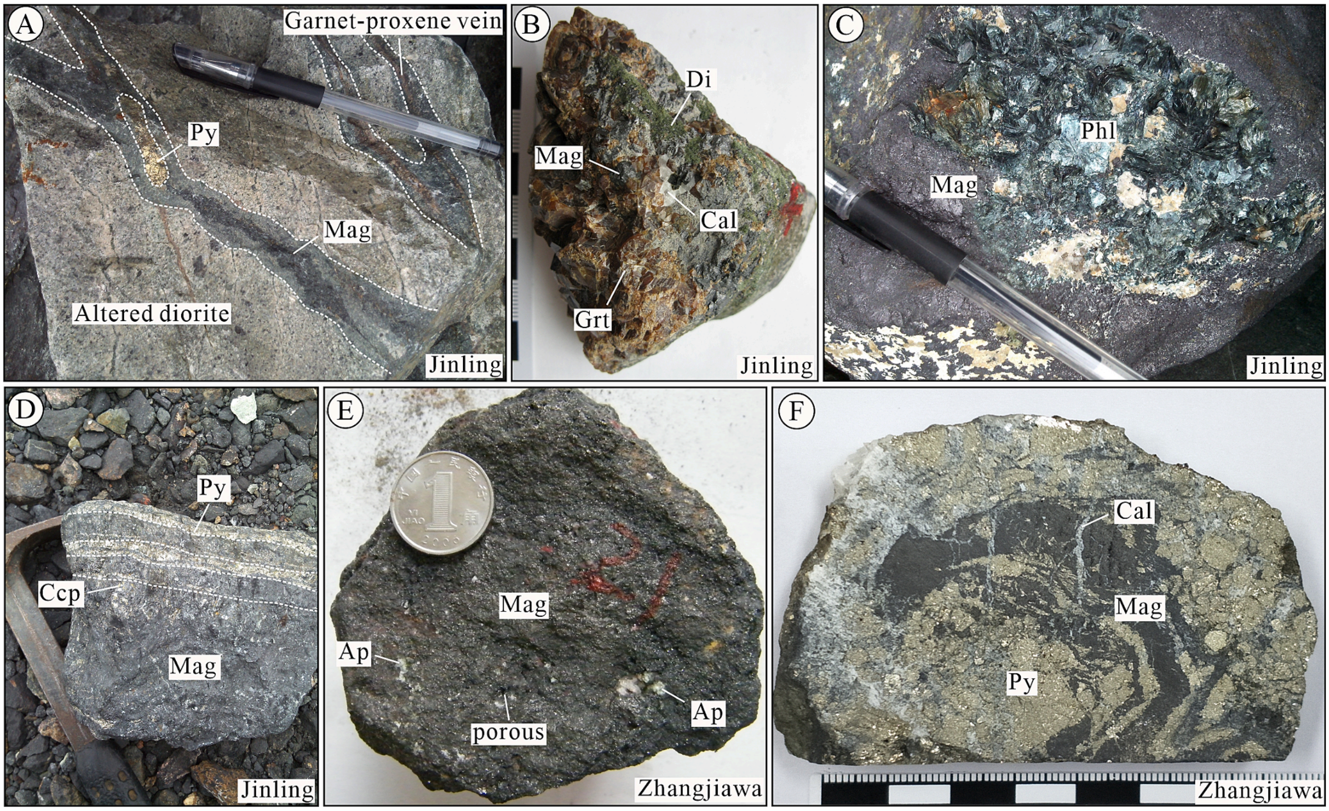

Fig. 3. Representative samples of different hydrothermal stages from the Jinling (A–D) and Zhangjiawa iron deposits (E–F). (A) Feldspathization of the ore-forming rock, which is cut by magnetite vein. The magnetite vein is overprinted by sulfide locally. (B) Garnet-diopside skarn from the prograde stage. (C) Massive magnetite ore from the retrograde stage, containing abundant phlogopite. (D) Massive magnetite ore cut by calcite-sulfide vein. (E) Massive magnetite ore, containing abundant apatite and showing porous texture. (F) Pyrite and calcite from the carbonate-sulfide stage, cutting and metasomatizing the massive magnetite ore. Abbreviations: Py = Pyrite; Mag = magnetite; Ap = Apatite; Cal = Calcite; Grt = Garnet; Di = Diopside, Ccp = Chalcopyrite; Phl = Phlogopite.

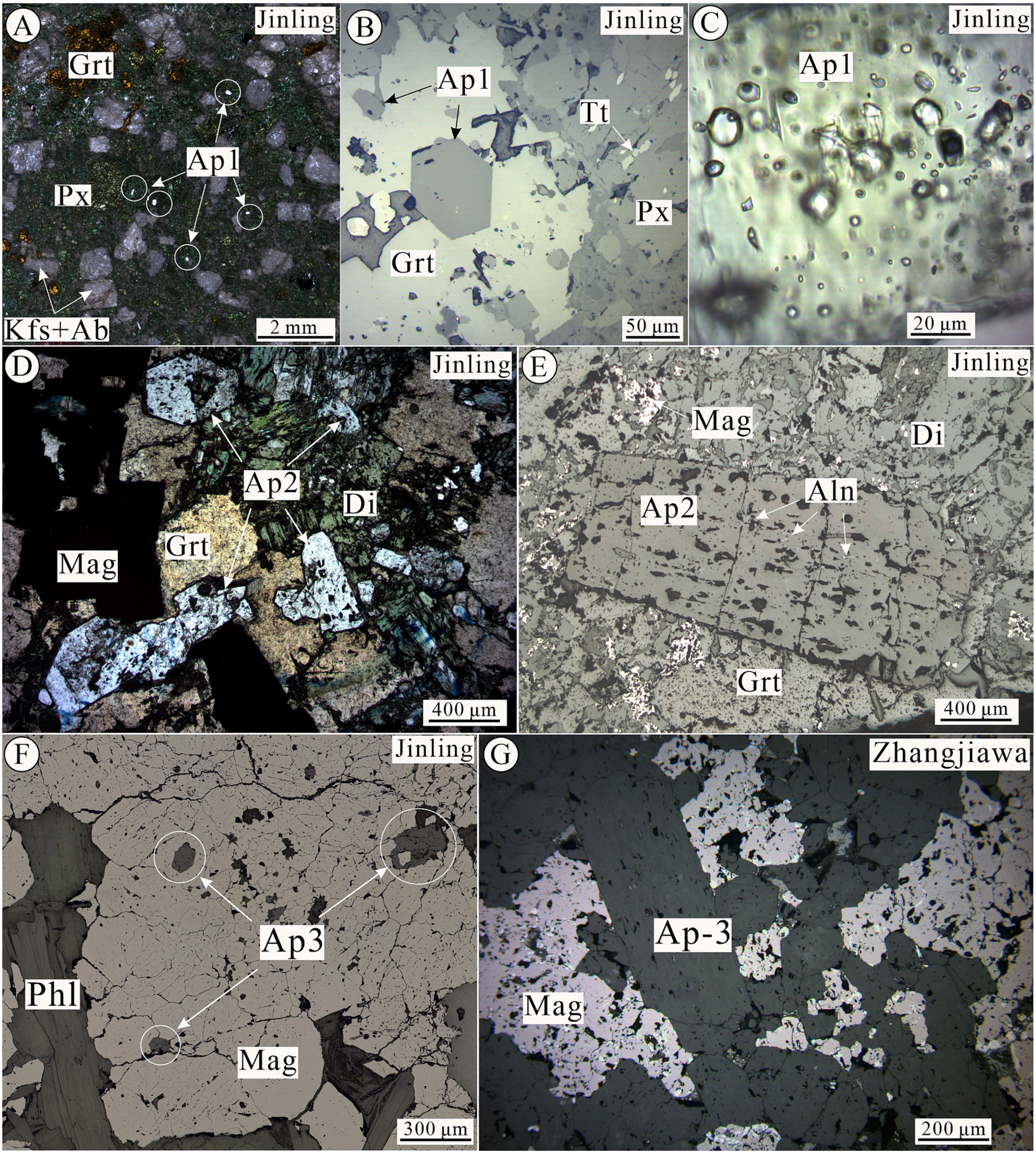

Fig. 4. Micrographs of apatite from the Jinling (A–F) and Zhangjiawa (G) iron deposits. (A) Ap1 apatite grains disseminated in the altered diorite (feldspathization) and coexisting with albite, K-feldspar, grandite garnet and clinopyroxene. (B) Euhedral Ap1 apatite grains intergrown with garnet, pyroxene and titanite. (C) Abundant fluid inclusions developed in the Ap1 apatite. (D) Ap2 apatite grains intergrown with garnet, diopside and minor magnetite. (E) Euhedral Ap2 apatite grain containing abundant allanite inclusions. (F) Ap3 apatite grains hosted in magnetite. (G) Ap-3 apatite grains intergrown with magnetite. (A), (C) and (D) are under transmitted light. (B), (E), (F) and (G) are under reflected light. Abbreviations: Px = Pyroxene; Kfs = K-feldspar; Tt = Titanite; Aln = Allanite; Others as in Fig. 3.

amalgamation among several Archean micro-continental blocks (Zhai and Santosh, 2011; Zhao et al., 2012) and after that, it remained largely stable until the Mesozoic, prior to the remarkable craton destruction at its central-eastern domains (Zhu et al., 2012). Large-scale mafic to felsic magmatic activities and various mineralization types (e.g., Au, Fe and Cu mineralization) were induced during the craton destruction (Li and Santosh, 2014).

The Luxi Block is located at the eastern part of the NCC, which is bounded by the Tan-Lu fault to the east, the Liaocheng-Lankao fault to the west, the Fengpei fault to the south and the Qihe-Guangrao fault to the north (Fig. 1B). The Tan-Lu fault extended deeply into the mantle, not only acting as a conduit for asthenospheric upwelling (Chen et al., 2006), but also controlling the emplacement of the widespread Mesozoic igneous rocks in the study region (Qiu et al., 2000; Ren et al., 2002). Gabbros, high-Mg diorites, high-K calc-alkaline to alkaline rocks, granites, basaltic to rhyolitic volcanic rocks, carbonatites and mafic dykes were developed during the early Cretaceous in this district (Lan et al., 2019). The high-Mg diorites, such as the Jinling intrusive complex in the Zibo area (Jin et al., 2015), the Kuangshan and Tietonggou intrusions in the Laiwu area (Duan and Li, 2017), the Tiezhai intrusive complex in the Linqu area and the Tongjing intrusion in the Yinan area (Zhang et al., 2011), were prone to generate Fe and Cu-Au skarn mineralization. The mineralization mainly occurred in the contact zones between the high-Mg diorites and the Paleozoic carbonate rocks.

3. Deposit geology

3.1. Jinling iron deposit

The Jinling iron deposit is located at the Zibo region, northern Luxi Block, and is associated with the Jinling high-Mg dioritic intrusions (Fig. 2A). It contains more than ten mining districts around the intrusions and hosts about 200 million tons of iron reserves with an average Fe grade of ~ 52 % (Jin et al., 2015). Orebodies are developed in the contact zones between the dioritic rocks and the Ordovician Majiagou and Carboniferous Benxi Formations. The strata are mainly composed of limestone, sandstones and sandy shales (Jin et al., 2015). The ore-related dioritic rocks cover an area of ~ 70 km^2, which consist of gabbroic diorite, monzodiorite and quartz monzonite. Zircon LA-ICP-MS U-Pb ages of the above rocks are 131.6 ± 0.8 Ma, 131.3 ± 0.6 Ma and 129.7 ± 0.8 Ma, respectively (Lan et al., 2019). Four principal hydrothermal stages have been recognized at the Jinling deposit, including the feldspathization, prograde skarn, retrograde skarn and calcite-sulfide stages. The feldspathization is mainly developed in the upper parts of the diorites with a thickness of ~ 50 m (Jin et al., 2015), where plagioclase phenocrysts were altered to albite and K-feldspar while amphibole and biotite were replaced by clinopyroxene, grandite garnet and titanite (Fig. 3A). Many (~1 vol%) apatite grains (Ap1) are disseminated in the altered rocks (Fig. 4A). In the prograde stage, skarns display a variable thickness of 0.5–20 m (Jin et al., 2015), which are mainly composed of grandite garnet, diopside and disseminated magnetite (Fig. 3B), with subordinate coarse-grained apatite (Ap2; Fig. 4D). LA-ICP-MS dating of the grandite garnet yielded an U-Pb age of ~ 129 Ma (Chen et al., 2021). In the retrograde stage, skarns are commonly 1 to 25 m thick and mainly consist of magnetite, phlogopite, epidote and amphibole (Fig. 3C), with subordinate fine-grained apatite (Ap3; Fig. 4F). Massive magnetite ores formed in this stage and are cut by the calcite-sulfide veinlets (Fig. 3D). Magnetite can also occur in narrow veins, which are locally overprinted by sulfides (Fig. 3A).

3.2. Zhangjiawa iron deposit

The Zhangjiawa iron deposit is located at the Laiwu region, northern Luxi Block, and is associated with the Kuangshan monzonite (Fig. 2B). It contains ~ 290 million tons of iron ores with an average Fe grade of ~ 46 wt% (Duan and Li, 2017). Orebodies mainly occur in the contact zones between the Kuangshan monzonite and the Middle Ordovician marine dolomite rocks with evaporite intercalations. LA-ICP-MS zircon U-Pb dating indicates that the Kuangshan monzonite was emplaced at 129.3 ± 0.3 Ma (Lan et al., 2019). On the basis of field and paragenetic relationships, four primary hydrothermal stages were recognized at the Zhangjiawa deposit, including the albitization, prograde skarn, retrograde skarn and carbonate-sulfide stages (Duan and Li, 2017; Chen et al., 2018). The albitization is extensively developed in the upper parts of the Kuangshan intrusion, where plagioclase and hornblende were typically replaced by fine-grained albite and scapolite (Duan and Li, 2017). The prograde skarns are developed in the exoskarn zone with a thickness of a few to tens of meters, which mainly consist of diopside (>80 vol%), spinel and forsterite (Duan and Li, 2017). The retrograde skarns are the major iron ores (massive magnetite ores; Fig. 3E), which mainly consist of magnetite, phlogopite and apatite (Ap-3; Fig. 4G), with subordinate serpentine, chlorite and titanite. Calcite and pyrite are developed in the carbonate-sulfide stage (Fig. 3F), which commonly cut or metasomatize the retrograde skarns.

4. Analytical methods

Representative apatite samples of different generations from the Jinling and Zhangjiawa Fe skarn deposits were collected. The samples were made into double-polished thin sections for SEM, EPMA and LA-ICP-MS analyses. In addition, sulfur isotopic analyses of sulfides from the two deposits were also conducted by isotope ratio mass spectrometer (IRMS).

4.1. SEM and EPMA analyses

Back-scattered electron (BSE) and cathodoluminescence (CL) images of apatite were acquired to check the microtexture. The analyses were conducted using a JSM-7800F SEM at the State Key Laboratory of Ore Deposit Geochemistry (SKLODG), Institute of Geochemistry, Chinese Academy of Sciences (IGCAS), Guiyang, China. The working conditions were 20 kV accelerating voltage and 10nA beam current.

Major elements of apatite were analyzed by a JOEL JXA 8230 EPMA at the SKLODG. The analytical conditions were 25 kV accelerating voltage, 10nA beam current and 3 ~ 10 μm beam size. The standards, analyzed elements and X-way lines were as follows: fluorapatite (F-Kα and P-Kα), chlorapatite (Cl-Kα, S-Kα, and Ca-Kα), orthoclase (Na-Kα and K-Kα), and pyrope (Mg-Kα, Si-Kα, Ti-Kα, Fe-Kα, and Cr-Kα). Peak and background counting times were 30 s and 15 s, respectively. Empirical apatite formulation was calculated based on 13 oxygen atoms per formula unit (apfu). X-position occupancies of volatiles were calculated using the measured F and Cl data while assuming $F + Cl + OH = 1$ for OH (Piccoli and Candela, 2002).

4.2. LA-ICP-MS trace element analysis

Trace element analysis of apatite was performed at the SKLODG by using an Agilent 7900 ICP-MS equipped with a Geolas Pro 193 nm ArF excimer laser ablation system. A helium flow rate of 450 mL/min was used to carry the ablated materials to the ICP. Argon was used as the makeup gas and mixed with the carrier gas via a T-connector before entering the ICP. An additional 3 mL/min N_2 gas was added downstream from the cell to enhance the signal sensitivity. A laser fluence of 4 J/cm^2, repetition rate of 6 Hz and spot size of 44 μm were used during the analyses. Each analysis incorporated of approximately 20 s gas blank followed by 40 s data acquisition from the sample and 20 s for washout. The CaO content determined by EPMA was employed as internal standard. The glass standards of NIST610 and NIST 612 were used as external standards for calibration. Each external standard was analyzed twice after eight sample analyses. Data processing was performed by the software *ICPMSDataCal* (Liu et al., 2008).

4.3. LA-ICP-MS U-Pb dating

In-situ U-Pb dating of apatite was also performed at the SKLODG using an Agilent 7900 ICP-MS equipped with a Geolas Pro 193 nm ArF excimer laser ablation system. A combination of 3.0 mL/min N_2 added downstream from the cell was adopted to enhance the signal sensitivity. A laser fluence of 4 J/cm^2, repetition of 6 Hz and spot size of 44 μm were used. The ICP-MS was tuned to reduce the oxide production ($^{248}ThO^+/^{232}Th^+ < 0.1\%$) and double changed ion production ($^{22}M^+/^{44}Ca^+ < 0.4\%$), maximize the sensitivities of the heavy masses (e.

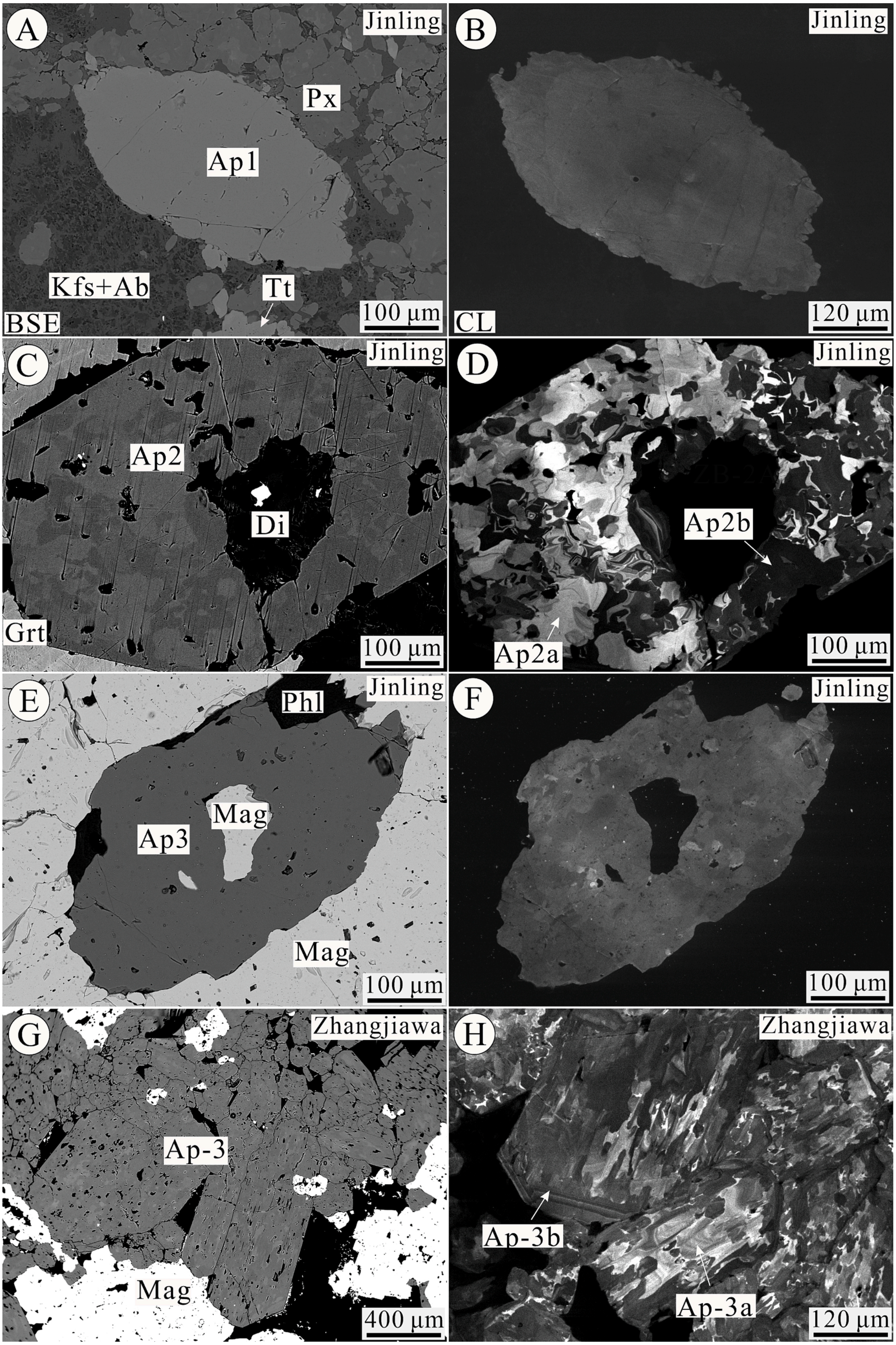

Fig. 5. Representative BSE (left) and CL (right) images of apatite from the Jinling and Zhangjiawa iron deposits. (A–B) Ap1 apatite showing homogenous texture. (C–D) Ap2 apatite showing patchy texture. (E–F) Ap3 apatite showing homogenous texture under BSE imaging and weak patchy texture under CL imaging. (G–H) Ap-3 apatite grains are porous under BSE imaging and show patchy texture under CL imaging.

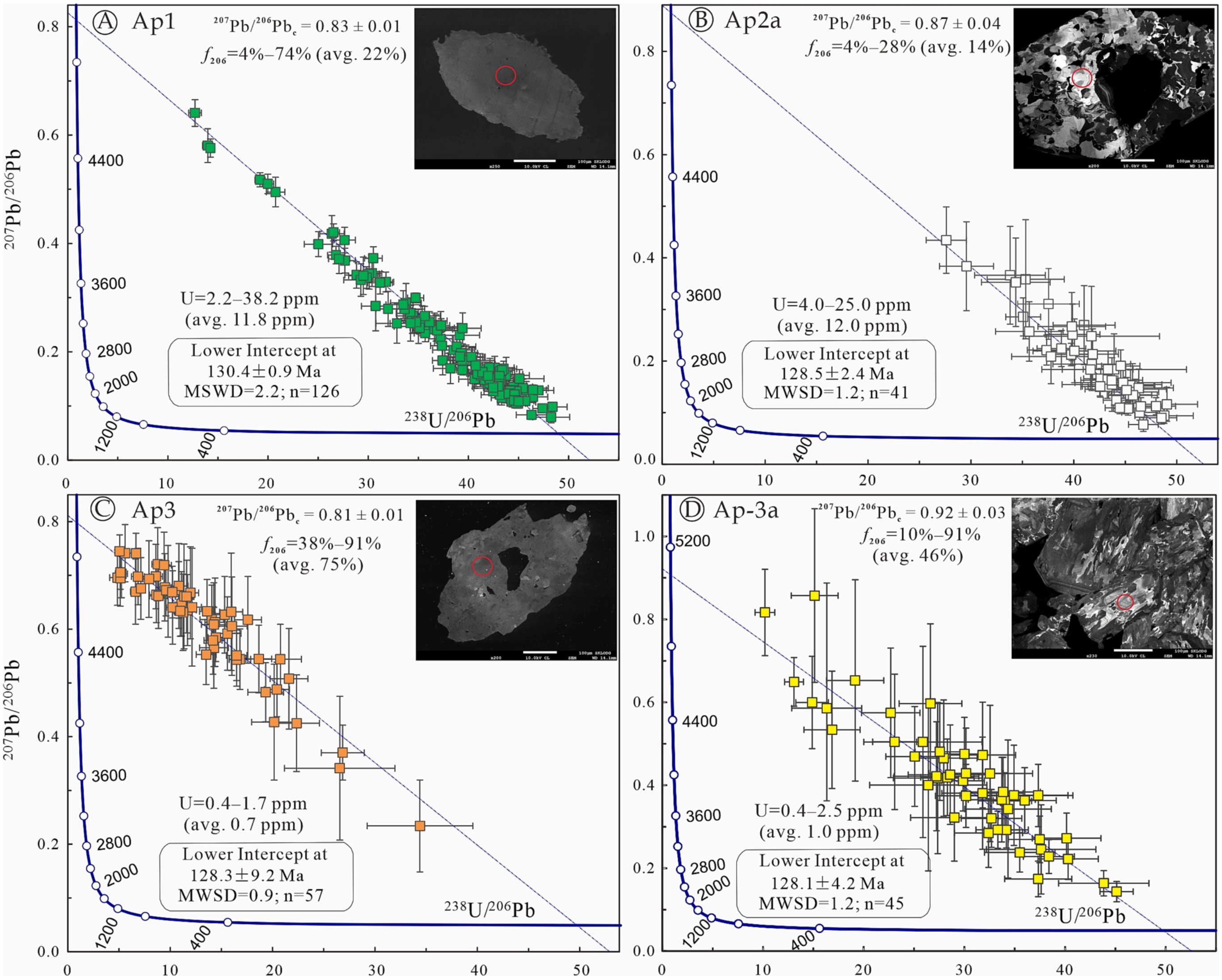

Fig. 6. Tera-Wasserburg Concordia diagrams of apatite from the Jinling (A–C) and Zhangjiawa iron deposit (D), showing the lower intercept U-Pb ages.

g., U, Th and Pb) and maintain the equal sensitivities of U and Th ($^{238}U^+/^{232}Th^+$ ratio of ∼ 1) (Chew et al., 2014; Fietzke and Frische, 2016). The dwell times were 6 ms for ^{43}Ca and ^{31}P, 10 ms for ^{202}Hg, ^{204}Pb, ^{208}Pb and ^{232}Th, 20 ms for ^{206}Pb and ^{238}U and 30 ms for ^{207}Pb. Each analysis incorporated of approximately 20 s gas blank followed by 40 s data acquisition. The matrix-matched OD306 apatite reference was utilized as primary standard for calibration (Thompson et al., 2016). The Madagascar (MAD2) apatite served as secondary standard for monitoring the data quality, which yielded a measured age of 474.6 ± 4.5 Ma during this study, well consistent with the recommended age (474.3 ± 0.4 Ma) (Thomson et al., 2012). Data reduction including off-line selection and integration of background and analyte signals, time-drift correction and quantitative calibrations were performed by *ICPMSDataCal* software (Liu et al., 2008). Because common Pb is commonly incorporated into apatite, the U-Pb age of apatite was obtained using the Tera-Wasserburg Concordia, where a linear regression through the plots yielded a lower intercept age (Tera and Wasserburg, 1972). The proportion of common Pb (f_{206}) was assessed through the methods of Gregory et al. (2007). Concordia diagrams and weighted mean calculations were processed using the *Isoplot* software (Ludwig, 2003).

4.4. Sulfur isotopic analysis

Sulfur isotopic analysis was also conducted at the SKLODG. Pure sulfide grains (pyrite and chalcopyrite) were hand-picked under binocular and then in-situ sampled using a microdrill sampling system (RELION MSS VI). The sampled sulfide powders were wrapped in a tin capsule and flash-combusted in a single reactor filled with WO_3 and Cu as reducing agents, liberating SO_2 during interaction with an O_2-enriched He gas. Isotopic measurements were conducted by a continuous-flow isotope ratio mass spectrometer (MAT253). International reference standards of IAEA-S-1, IAEA-S-2 and IAEA-S-3 were used as external standards, with the analytical precisions better than ± 0.2‰. The S isotopic composition is expressed against the Vienna Canyon Diablo Troilite (V-CDT) international standard.

5. Results

5.1. Petrography and microtexture of apatite

5.1.1. Apatite from the Jinling deposit

Three generations of apatite (Ap1, Ap2 and Ap3) are developed in the Jinling deposit, which occur in the feldspathization, prograde and retrograde stages, respectively. The Ap1 apatite grains are disseminated

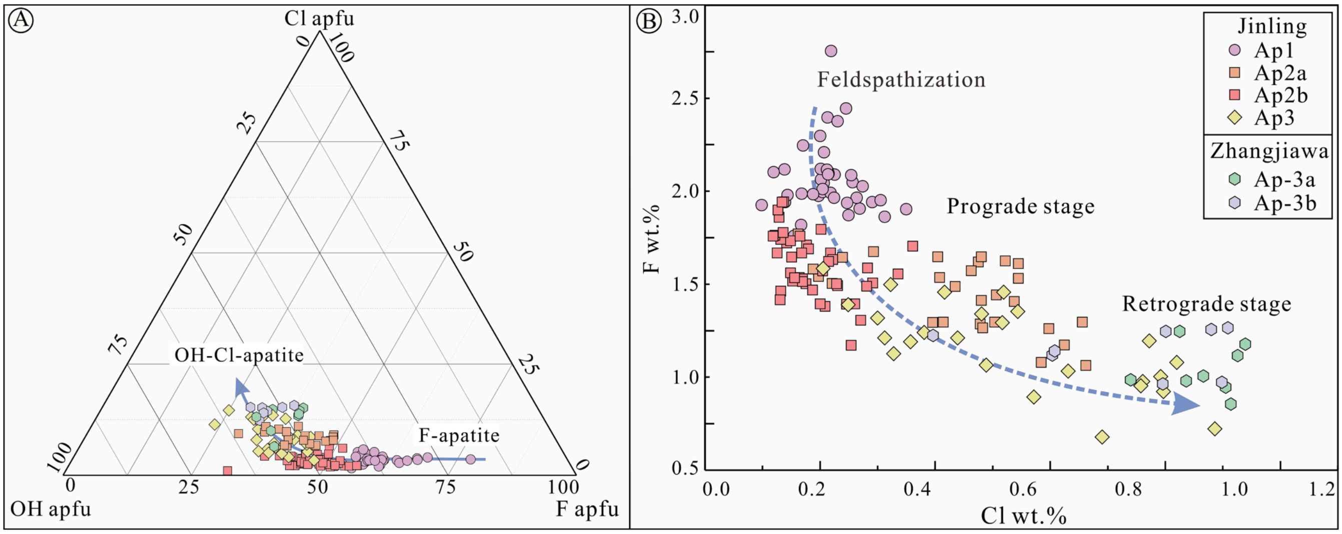

Fig. 7. Halogen concentrations in apatite from the Jinling and Zhanjiawa iron deposits. (A) Ternary plot in terms of F-Cl-OH atomic proportions, calculated using the method of Piccoli and Candela (2002). (B) Covariant plot for F and Cl concentrations.

in the altered diorite and commonly coexist with albite, K-feldspar, grandite garnet and clinopyroxene (Fig. 4A, B). These apatite grains are euhedral to subhedral with variable sizes of 50–400 μm. They typically contain abundant fluid inclusions (Fig. 4C), and display homogeneous texture under both the BSE and CL imaging (Fig. 5A, B). The Ap2 apatite grains are euhedral to subhedral with larger sizes of 0.2–3 mm. These apatite grains are intergrown with garnet, diopside and magnetite (Fig. 4D). Under the BSE and CL imaging, patchy texture showing bright and dark zones is featured in these apatite grains (Fig. 5C, D). The bright zones (Ap2a) are more homogeneous and seem to be residues, whereas the dark zones (Ap2b) metasomatize the bright zones and contain mineral inclusions such as allanite (Fig. 4E). The Ap3 apatite grains are euhedral to subhedral with sizes of 30–200 μm. These apatite grains commonly occur as inclusions in magnetite (Fig. 4F), and contain magnetite inclusions as well (Fig. 5E). They show homogeneous texture under the BSE imaging (Fig. 5E), but show weak patchy texture under the CL imaging (Fig. 5F).

5.1.2. *Apatite from the Zhangjiawa deposit*

One generation of apatite is developed in the Zhangjiawa deposit, which occurs in the massive magnetite ores. Petrographically, this generation of apatite is comparable to the Ap3 in the Jinling deposit and

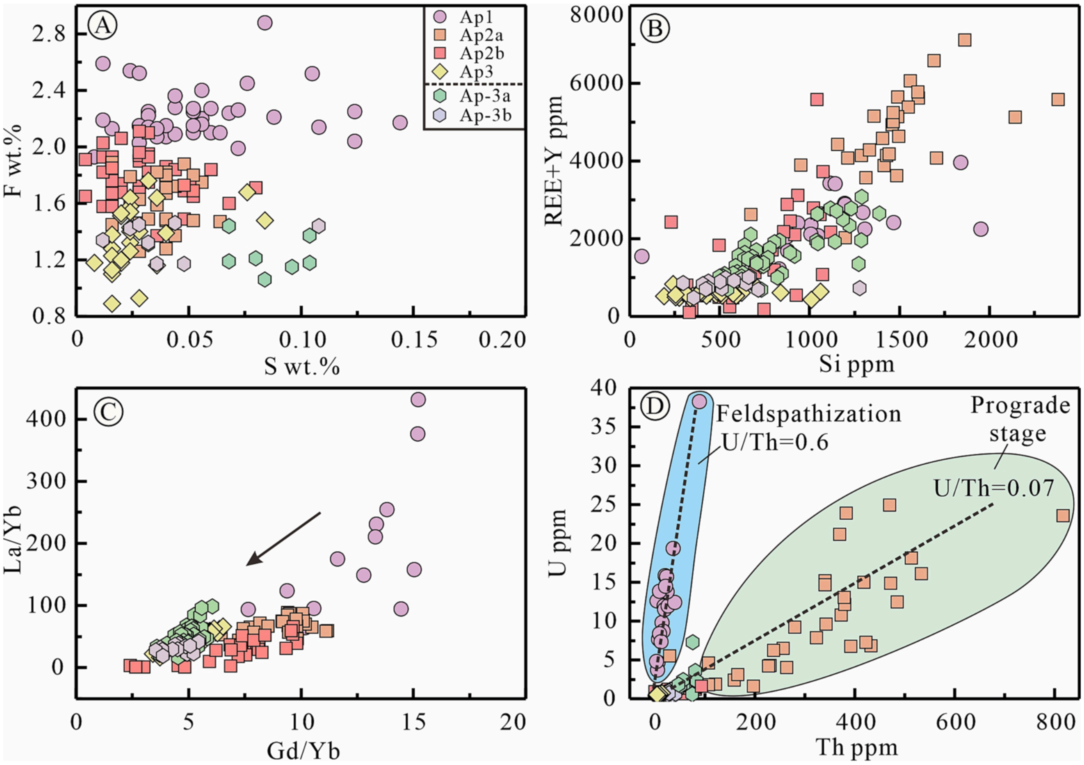

Fig. 8. Covariant plots for different elements and elemental ratios in apatite. (A) Plot of F vs. S concentrations. (B) Plot of (REE + Y) vs. Si concentrations. (C) Plot of chondrite-normalized La_N/Yb_N vs. Gd_N/Yb_N ratios. (D) Plot of U vs. Th concentrations.

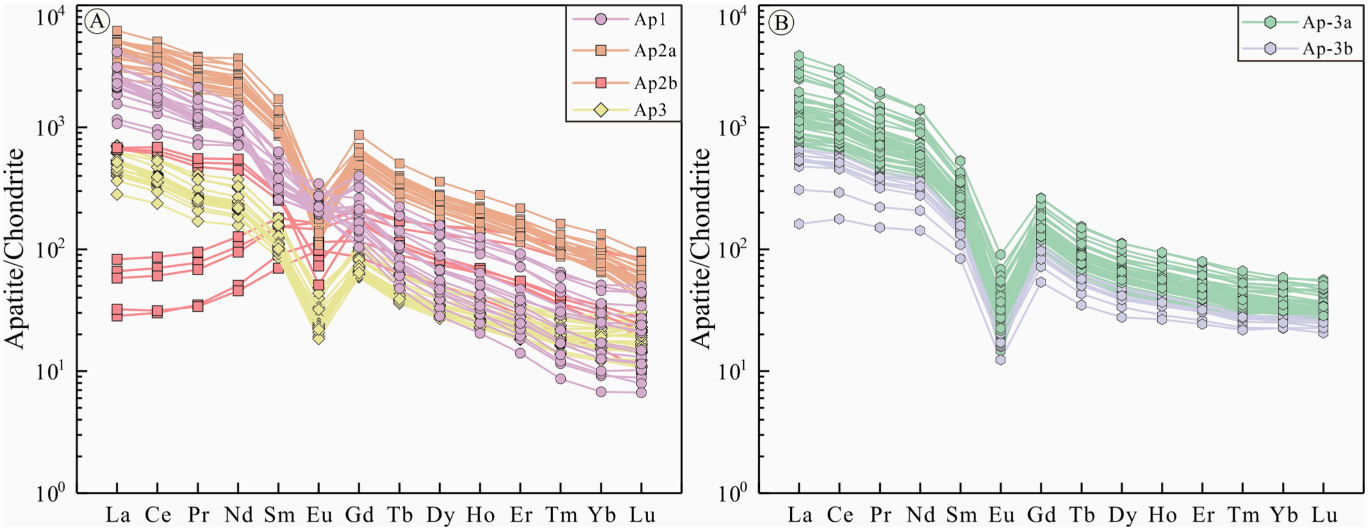

Fig. 9. Chondrite-normalized REE patterns for the apatite from the Jinling (A) and Zhangjiawa (B) iron deposits.

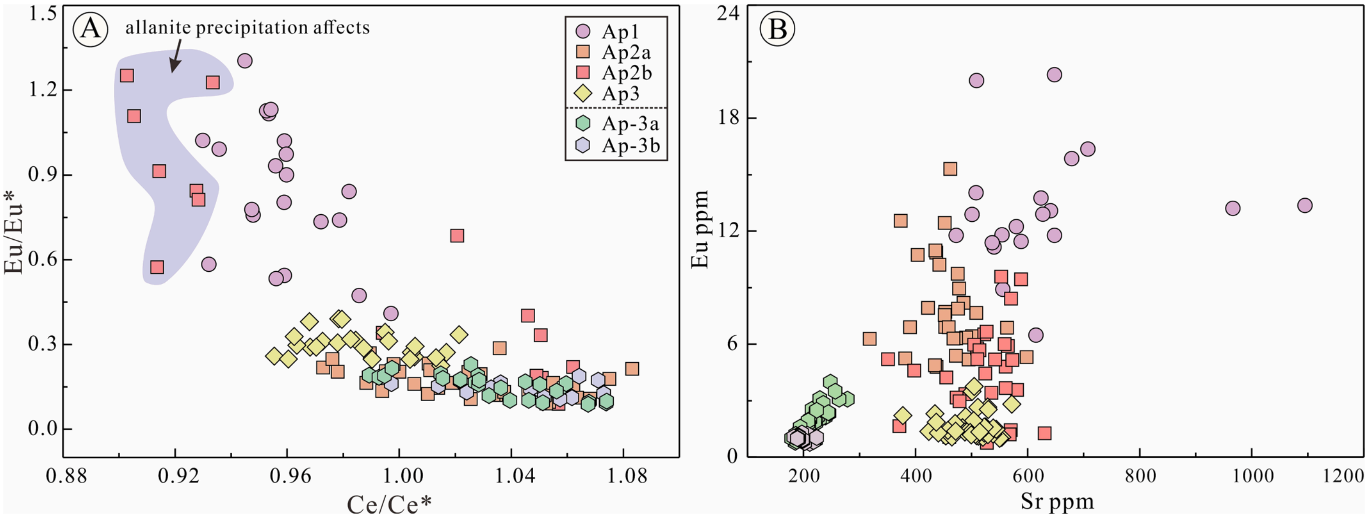

Fig. 10. Plots of Eu/Eu* vs. Ce/Ce* ratios (A) and Eu vs. Sr concentrations (B) in apatite from the Jinling and Zhangjiawa iron deposits. Eu/Eu*=$Eu_N \times (Sm_N \times Gd_N)^{-0.5}$ and Ce/Ce*=$Ce_N \times (La_N \times Pr_N)^{-0.5}$.

thus named as Ap-3. The Ap-3 apatite grains are euhedral to subhedral with variable sizes of 100–1500 μm. They coexist with magnetite and contain tiny magnetite inclusions (Fig. 4G). They are porous under the BSE imaging (Fig. 5G), and show patchy texture under the CL imaging (Fig. 5H). The patchy texture consists of bright (Ap-3a) and dark (Ap-3b) zones, of which the bright zones seem to be the residues while the dark zones are the altered ones.

5.2. U-Pb age of apatite

The U-Pb dating results of apatite are summarized in Table S1 and plotted in Fig. 6. One hundred and twenty-six analyses of the Ap1 yield a Tera-Wasserburg Concordia lower intercept age of 130.4 ± 0.9 Ma (MSWD = 2.2, 2σ) (Fig. 6A). The Ap2 apatite grains were partly altered, of which the unaltered grains or zones (Ap2a) were selected for dating. Forty-one analyses of the Ap2a yield a Tera-Wasserburg Concordia lower intercept age of 128.5 ± 2.4 Ma (MSWD = 1.2, 2σ) (Fig. 6B). Fifty-seven analyses of the Ap3 yield a Tera-Wasserburg Concordia lower intercept age of 128.3 ± 9.2 Ma (MSWD = 0.9, 2σ) (Fig. 6C). Forty-five analyses of the Ap-3a yield a Tera-Wasserburg Concordia lower intercept age of 128.1 ± 4.2 Ma (MSWD = 1.2, 2σ) (Fig. 6D).

Notably, the Ap3 and Ap-3a show much higher uncertainties of U-Pb age than those of the Ap1 and Ap2a. This could be due to their remarkably low U contents (<3 ppm) and high proportions of common Pb (average $f_{206} > 40\%$) (Fig. 6). In addition, the altered grains or zones (commonly darker in CL imaging) have lower U contents and higher proportions of common Pb than those of the unaltered, indicating that deuteric modification affected the U-Pb age.

5.3. Geochemistry of apatite

The elemental compositions of apatite are listed in Table S1 and shown in Figs. 7–10.

5.3.1. Apatite from the Jinling deposit

For halogens, the F concentrations decrease from the Ap1 (1.93–2.88 wt%, mean of 2.22 wt%) to the Ap2a (1.26–1.88 wt%, mean of 1.60 wt%) and then to the Ap3 (0.89–1.76 wt%, mean of 1.35 wt%), whereas the Cl concentrations show an opposite trend, increasing from 0.11–0.40 wt% (mean of 0.25 wt%) to 0.42–0.76 wt% (mean of 0.58 wt %) and then to 0.24–1.02 wt% (mean of 0.61 wt%), correspondingly (Fig. 7). The sulfur contents show a consistent trend with F, decreasing

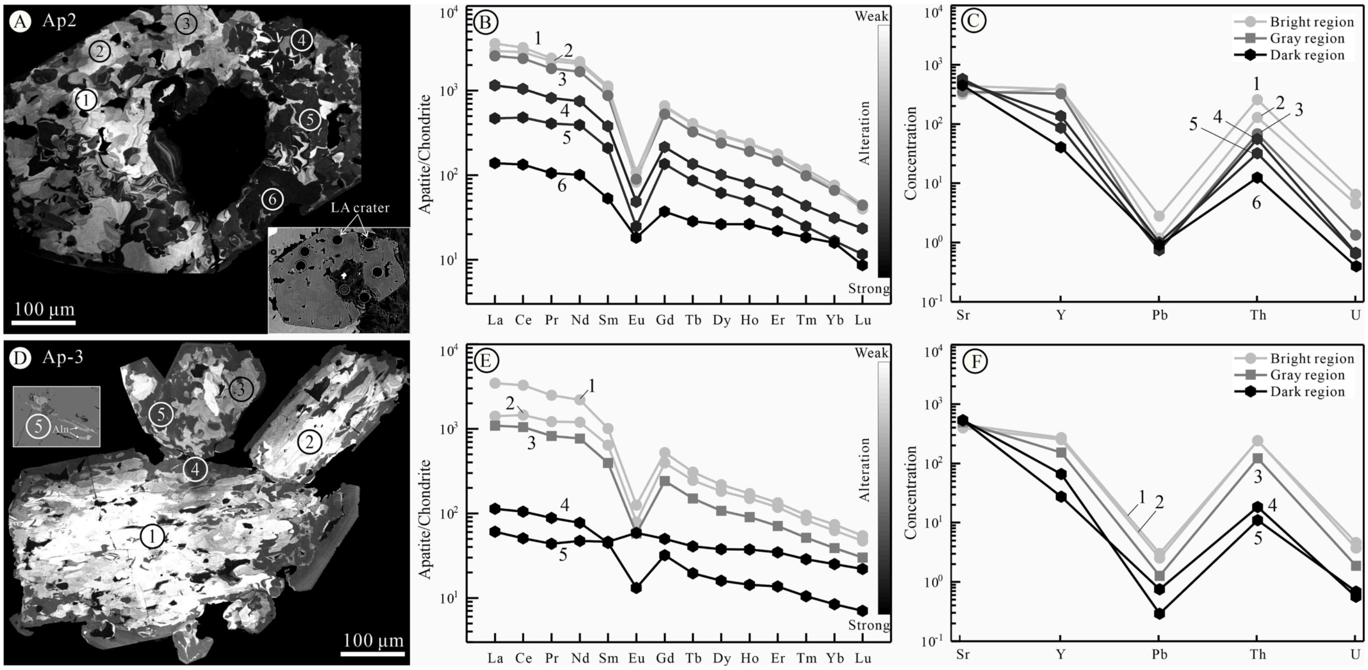

Fig. 11. Variations of REE and trace elements (Sr, Y, Pb, Th and U) from CL-bright to dark zones in the Ap2 (A–C) and Ap-3 (D–F) apatite grains, showing the continuous loss of elements with increasing alteration. The number and circle indicate the spot of laser ablation.

from the Ap1 (0.01–0.25 wt%, mean of 0.06 wt%) to the Ap2a (0.02–0.06 wt%, mean of 0.04 wt%) and then to the Ap3 (0.00–0.08 wt %, mean of 0.03 wt%) (Fig. 8A).

The REE + Y contents increase from the Ap1 (1202–3920 ppm, mean of 2348 ppm) to the Ap2a (1887–6670 ppm, mean of 4312 ppm), but decrease significantly to the Ap3 (346–794 ppm, mean of 552 ppm) (Fig. 8B). The Ap1 apatite grains show much stronger fractionation between LREE and HREE ($La_N/Yb_N = 20$–408) with weaker negative Eu anomalies (Eu/Eu*=0.4–1.3) than those of the Ap2a ($La_N/Yb_N = 15$–60, Eu/Eu*=0.1–0.3) and Ap3 ($La_N/Yb_N = 14$–42, Eu/Eu*=0.2–0.4) (Fig. 8C, 9A, 10A). The U and Th concentrations are the highest in the Ap2a (U = 4.0–25.0 ppm, Th = 108–839 ppm) while lowest in the Ap3 (U = 0.4–1.7 ppm, Th = 3.4–22.8 ppm), and vary widely in the Ap1 (U = 2.2–38.2 ppm, Th = 2.5–94.5 ppm). The U/Th ratios in the Ap1 (U/Th = 0.6) are much higher than those in the Ap2a and Ap3 (U/Th = 0.07) (Fig. 8D).

The altered (Ap2b) and unaltered (Ap2a) grains or zones have distinct elemental compositions, showing that the Cl, Na, Si, REEs, Pb, Th and U contents are lower but the F, Sr, Ca and P contents are higher in the former (Figs. 7–11, Table S1). Some trace elements such as REEs + Y, U, Th and Pb decrease continuously with increasing alteration (Fig. 11).

5.3.2. Apatite from the Zhangjiawa deposit

The F, Cl and S concentrations in the Ap-3a are 1.06–1.44 wt%, 0.85–1.08 wt% and 0.03–0.10 wt%, respectively, while in the Ap-3b are 1.17–1.46 wt%, 0.46–1.05 wt% and 0.01–0.11 wt% (Table S1). The F and S contents do not show significant difference, but the Cl contents decrease from the Ap-3a to the Ap-3b. The apatite grains from the Zhangjiawa deposit have systematically higher Cl but lower F contents than those of the Jinling deposit (Fig. 7B).

The REE + Y concentrations of Ap-3a (1004–2950 ppm, mean of 1650 ppm) are higher than those of the Ap-3b (423–959 ppm, mean of 773 ppm) (Fig. 8B), but they have similar REE distribution patterns (Fig. 9B). Both of them show significant fractionation between LREE and HREE ($La_N/Yb_N = 22$–67, avg. 37) (Fig. 8C) and strong negative Eu anomalies (Eu/Eu*=0.1–0.2) (Fig. 10A).

5.4. Sulfur isotopic compositions of sulfides

Sulfur isotopic compositions of sulfides are listed in Table 1. The $\delta^{34}S_{V\text{-}CDT}$ values of pyrite and chalcopyrite in the Jinling deposit vary widely from 0.0‰ to 10.1‰ (mean of 6.7‰) and 3.6‰ to 10.8‰ (mean of 6.4‰), respectively. By contrast, the $\delta^{34}S_{CDT}$ values of pyrite and chalcopyrite in the Zhangjiawa deposit are quite consistent and are much higher than those of the Jinling deposit, showing the values of 16.4–20.9‰ and 20.4–21.1‰, respectively.

6. Discussion

6.1. Origin of the ore-forming fluids and metals

The U-Pb ages of apatite from the Jinling deposit vary between 128.3 Ma and 130.4 Ma (Fig. 6A–C), which are in good agreement with the zircon U-Pb age of the spatially associated quartz monzonite (130.1 ± 1.5 Ma, Lan et al., 2019). The apatite U-Pb age of the Zhangjiawa deposit is 128.1 ± 4.2 Ma (Fig. 6D), also consistent with the zircon U-Pb age of the spatially associated Kuangshan monzonite within errors (129.5 ± 0.6 Ma, Lan et al., 2019). Compared with other gabbroic to dioritic rocks in the study region, the above rocks have the lowest H_2O and highest SiO_2 contents and highest Mg# values (100 × Mg/(Mg+∑Fe) molar ratio > 60, Lan et al., 2019). This indicates that remarkable exsolution of fluids and metals (Fe) from these rocks occurred. In combination with the skarn-type mineralization, it is clear that the ore-forming fluids and metals were originally derived from these high-Mg rocks. Notably, sedimentary materials containing carbonates and shales have been identified in these rocks, which were considered to play a significant role in promoting fluid and metal exsolution (Lan et al., 2019). The carbonates can provide abundant CO_2 to promote the H_2O to be partitioned into the fluids (Holloway, 1976; Meinert et al., 2005), whereas the shales can reduce the originally oxidized magmas and create suitable oxygen fugacity for the extraction and transportation of Fe^{2+} by fluids (Lan et al., 2019).

Table 1
Sulfur isotopic data of sulfides from the Jinling and Zhangjiawa iron deposits.

Sample No.	Deposit	Mineral	$\delta^{34}S_{V\text{-}CDT}$(‰)	Source
Py-1	Jinling	Pyrite	7.3	This study
Py-2	Jinling	Pyrite	7.2	This study
Py-3	Jinling	Pyrite	6.4	This study
Py-4	Jinling	Pyrite	6.7	This study
Py-5	Jinling	Pyrite	9.5	This study
Py-6	Jinling	Pyrite	6.3	This study
Py-7	Jinling	Pyrite	5.2	This study
Py-8	Jinling	Pyrite	5.8	This study
Py-9	Jinling	Pyrite	9.9	This study
Py-10	Jinling	Pyrite	7.2	This study
Py-11	Jinling	Pyrite	7.2	This study
Py-12	Jinling	Pyrite	10.1	This study
Py-13	Jinling	Pyrite	6.1	This study
Py-14	Jinling	Pyrite	0.0	This study
Py-15	Jinling	Pyrite	5.4	This study
Ccp-1	Jinling	Chalcopyrite	9.0	This study
Ccp-2	Jinling	Chalcopyrite	10.8	This study
Ccp-3	Jinling	Chalcopyrite	7.7	This study
Ccp-4	Jinling	Chalcopyrite	3.6	This study
Ccp-5	Jinling	Chalcopyrite	5.4	This study
Ccp-6	Jinling	Chalcopyrite	4.5	This study
Ccp-7	Jinling	Chalcopyrite	3.9	This study
Py-1	Zhangjiawa	Pyrite	19.3	This study
Py-2	Zhangjiawa	Pyrite	19.8	This study
Py-3	Zhangjiawa	Pyrite	19.2	This study
Py-4	Zhangjiawa	Pyrite	19.5	This study
Py-5	Zhangjiawa	Pyrite	17.2	This study
Py-6	Zhangjiawa	Pyrite	16.4	This study
Py-7	Zhangjiawa	Pyrite	18.1	This study
Py-8	Zhangjiawa	Pyrite	16.5	This study
Py-9	Zhangjiawa	Pyrite	20.1	This study
Py-10	Zhangjiawa	Pyrite	20.9	This study
Py-11	Zhangjiawa	Pyrite	19.7	This study
Py-12	Zhangjiawa	Pyrite	19.7	This study
Py-13	Zhangjiawa	Pyrite	20.8	This study
Py-14	Zhangjiawa	Pyrite	18.9	This study
Py-15	Zhangjiawa	Pyrite	19.2	This study
Ccp-1	Zhangjiawa	Chalcopyrite	20.4	This study
Ccp-2	Zhangjiawa	Chalcopyrite	21.1	This study
Anh-1	Zhangjiawa	Ordovician gypsum	27.8	Duan, 2019
Anh-2	Zhangjiawa	Ordovician gypsum	27.3	Duan, 2019
Anh-3	Zhangjiawa	Ordovician gypsum	26.9	Duan, 2019
Anh-4	Zhangjiawa	Ordovician gypsum	28.6	Duan, 2019

6.2. Fluid evolution and Fe mineralization

6.2.1. Exsolution and transportation of Fe

Efficient exsolution of metals from melts is critical for forming the magmatic-hydrothermal deposits, which typically depends on the transporting agents such as Cl, F and S (e.g., Heinrich et al., 1999; Williams-Jones and Heinrich, 2005; Seo et al., 2009; McPhie et al., 2011; Williams-Jones and Migdisov, 2014; Xing et al., 2019; Alex and Zajacz, 2022; Gammons and Allin, 2022). Numerous studies have shown that in the high-temperature magmatic-hydrothermal fluids Fe is mainly transported as Fe-Cl complexes ($FeCl_2$ and $FeCl_4^{2-}$, Simon et al., 2004; Bell and Simon, 2011; Xing et al., 2019), implying that the extraction of Fe from the melts is mainly associated with the Cl-bearing fluids. However, in the studied deposits, all the apatite grains have the F/Cl ratios higher than 1, and show decreasing F and increasing Cl concentrations from the early to the late hydrothermal stages (Fig. 7B). This indicates that the originally exsolved fluids were more enriched in F. High F concentrations and F/Cl ratios of apatite have been widely identified in the ore-related magmatic-hydrothermal systems (e.g., Chang and Meinert, 2008; McPhie et al., 2011; Cao et al., 2012; Migdisov and Williams-Jones, 2014). The roles of F in magmatic-hydrothermal systems were estimated by previous studies (Xing et al., 2019 and references therein), which at least include: (1) increasing the solubility of metals by forming stable aqueous complexes; (2) acting as a precipitating agent; (3) reflecting the source of the ore-forming fluids; and (4) promoting metal leaching. Because in the mixed F-Cl solutions Fe(II)-Cl complexes are predominant at temperatures higher than 200 °C while Fe(III)-F complexes are significant at low temperatures (≤150℃) (Xing et al., 2019), the elevated F concentrations in the early hydrothermal fluids (Ap1 stage) might not contribute to extract and transport Fe. By contrast, considering that F can enhance the porosity of the wallrocks by breaking the Si-O bond in silicates and thus promote the metal leaching (Chang and Meinert, 2008; McPhie et al., 2011; Xing et al., 2019), it is inferred that large amounts of Fe were leached from the ore-forming rocks due to the F destroying the Fe-bearing silicates. This might be critical for the elevated enrichment of Fe in the ore-forming fluids.

6.2.2. Physicochemical variations and Fe precipitation

As the dominant species in the magmatic-hydrothermal fluids, the breakdown of Fe(II)-Cl complexes can be induced by the change of physicochemical conditions such as temperature, pressure, pH and Eh (e.g., Seward and Barnes, 1997; Wood and Samson, 1998; Simon et al., 2004; Yardley, 2005; Williams-Jones et al., 2010; Shu et al., 2017). In both the Jinling and Zhangjiawa deposits, the Ap3 and Ap-3a apatite grains in the massive magnetite ores have the highest Cl concentrations (Fig. 7B). This might imply the decoupling of Cl and Fe, which resulted in the efficient deposition of Fe. Experimental and thermodynamic modeling studies show that the solubilities of Fe-Cl complexes in hydrothermal fluids decrease sharply as temperature decreases from ~ 400 °C to 200 °C (Xing et al., 2019). Because cooling would inevitably occur during the magmatic-hydrothermal evolution, it is no doubt that cooling contributed to the deposition of Fe. However, besides the temperature, other factors seem to also promote the Fe deposition. Magnetite is the dominant ore mineral in the studied deposits, the formation of which requires increasing oxygen fugacity to oxidize Fe^{2+} to Fe^{3+}. Europium and Ce in apatite can reflect the redox condition of the crystallization environment (Cao et al., 2012; Pan et al., 2016; Mercer et al., 2020), of which Eu^{3+} and Ce^{3+} are more favorably incorporated into the apatite than Eu^{2+} and Ce^{4+} due to their similar radii to Ca^{2+} (Sha and Chappell, 1999). As a result, apatite crystallizing in more oxidized environment will have higher Eu but lower Ce contents, or show positive Eu anomaly (Eu/Eu*) and negative Ce anomaly (Ce/Ce*) (Mercer et al., 2020). The Eu/Eu* values increase from the Ap2a to the Ap3 while the Ce/Ce* values decrease accordingly (Fig. 10A), corroborating the increasing oxygen fugacity. It is noted that the Ap1 apatite grains have remarkably higher Eu/Eu* and lower Ce/Ce* values than those of the Ap2a and Ap3 (Fig. 10A), which cannot be explained by the high oxygen fugacity. Firstly, almost no oxidative minerals (e.g., magnetite and sulfate) occur in the Ap1 stage. Secondly, relatively low oxygen fugacities have been identified in the ore-forming rocks (Lan et al., 2019), implying the low oxygen fugacities of the exsolved fluids. It has been considered that the low oxygen fugacity during the magmatic-hydrothermal transition can not only make the Fe retain in the melts as Fe^{2+}, but also facilitate it to be scavenged by the fluids as Fe(II)-Cl complexes (Lan et al., 2019). Previous studies show that feldspar can significantly elevate the Eu concentrations and Eu/Eu* values of apatite when they are coexistent (Pan et al., 2016; Xiao et al., 2021). The Ap1 apatite grains occur in the feldspathization (Fig. 4A and 10A), and have the highest Sr and Eu concentrations (Fig. 10B), corroborating the effects of feldspar. For the Ce anomaly, due to the extremely small proportion of Ce^{4+} compared with Ce^{3+}, the Ce anomaly in apatite can be very small and thus cannot well indicate the oxidation state (Xing et al., 2021). This alerts that it should be cautious when applying the Eu/Eu* and Ce/Ce* as redox indicators (Xing et al., 2021).

The S concentrations in apatite decrease continuously from the Ap1 to the Ap2a and then to the Ap3 (Fig. 8A), also indicating the increasing oxygen fugacity. It has been demonstrated that there are three S oxidation states (S^{6+}, S^{4+} and S^{2-}) in the apatite, of which the S^{2-} occurs in reduced conditions while the S^{4+} and S^{6+} occur in intermediate to oxidized conditions (Konecke et al., 2017). Sulfides (mainly pyrite)

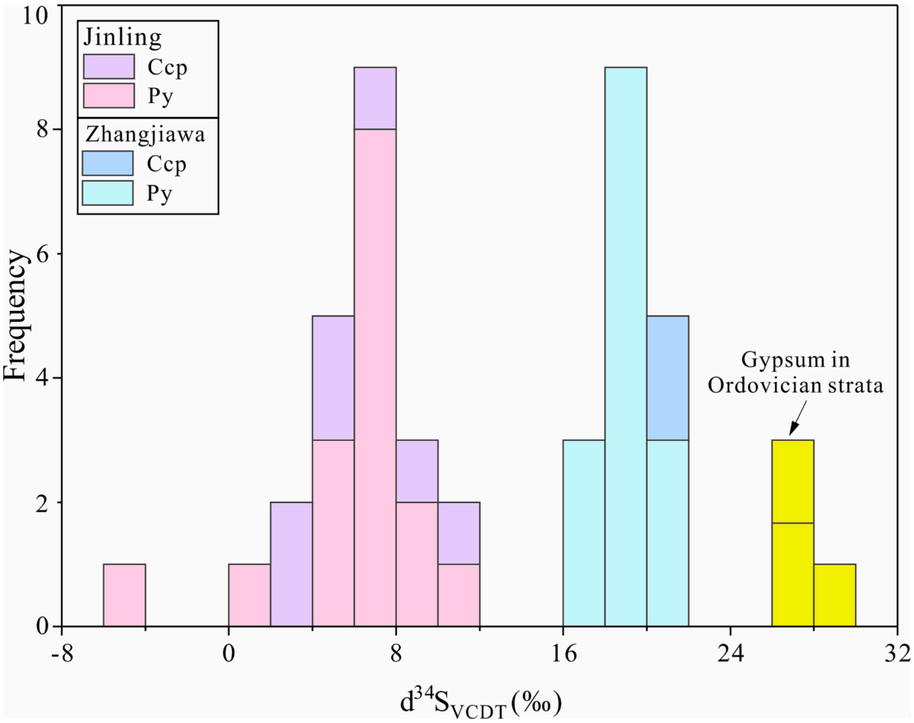

Fig. 12. Histogram of $\delta^{34}S_{V\text{-}CDT}$ for sulfides from the Jinling and Zhangjiawa iron deposits. The $\delta^{34}S_{V\text{-}CDT}$ values of gypsum in Ordovician strata are from Duan (2019).

coexisting with magnetite and apatite (Ap3 and Ap-3 stages) were identified in the massive magnetite ores of the Jinling and Zhangjiawa deposits (Fig. 3D and F), indicating that the oxygen fugacities of the fluids were around the magnetite-pyrite buffer during the deposition of Fe. Combined with no sulfates occurring throughout the hydrothermal stages, the S most likely presented as reduced species (S^{2-}) in the fluids (Henning et al. 2000; Seo et al., 2009; Simon and Ripley, 2011; Konecke et al., 2017) and thus as S^{2-} in the apatite. If it is true, the decreasing S concentrations in the apatite should be resulted from the deposition of sulfides, implying the oxidation of HS^- or S^{2-} to S^-.

The increase of oxygen fugacity was probably induced by fluid-rock interaction. It is noted that the Ap3 apatite grains have much higher Sr concentrations than those of the Ap-3a (Fig. 10B). Strontium can be incorporated into apatite via substituting Ca due to the similar ion radii and valence between Ca^{2+} and Sr^{2+} (Pan and Fleet, 2002). The higher Sr concentrations in the Ap3 apatite grains may indicate the crystallization in Ca-rich environments. This is corroborated by the wallrocks in the studied deposits, where limestones are developed in the Jinling deposit while dolomites occur in the Zhangjiawa deposit. The limestones can provide abundant Ca^{2+} and Sr^{2+} into the fluids during fluid-rock interaction. The different wallrocks and their effects can also be reflected by the sulfur isotopic compositions of sulfides. The $\delta^{34}S$ values of sulfides from the Zhangjiawa deposit range 16.4‰ from 21.1‰, much higher than those (0.0‰ to 10.8‰) of the Jinling deposit (Fig. 12). This is consistent with the widespread Ordovician marine strata in the Zhangjiawa deposit, which contain high-$\delta^{34}S$ sulfates (Wen et al., 2017; Duan, 2019).

6.3. Fluid metasomatism and effects on Fe grade

Both the Ap2 and Ap-3 apatite grains show patchy textures, which consist of residual bright zones (Ap2a and Ap-3a) and newly formed grey to dark zones (Ap2b and Ap-3b) under the CL imaging. In addition, the bright zones are commonly porous while the dark zones contain many mineral inclusions (Figs. 4, 5). These features have been considered to reflect the dissolution-reprecipitation processes during metasomatism (e.g., Harlov et al., 2002, 2005; Harlov and Förster, 2003; Li and Zhou, 2015). Based on the brightness, the REE + Y, Pb, Th and U contents decrease continuously from the bright to the grey and then to the dark zones (Fig. 11), indicating the enhanced loss of the above elements during increasing metasomatism. Notably, the bright zones have much stronger fractionation between LREE and HREE than those of the dark zones (Fig. 8C and 9). This suggests that the light rare earth elements were more easily mobilized during the metasomatism, as indicated by the newly formed LREE-rich allanite inclusions in the dark zones (Fig. 4E and 11D). To form the allanite [$(Ca, REE)_2FeAl_2Si_3O_{12}(OH)$], sufficient LREE and Ca are required (Budzyń et al., 2011). The Ap2a apatite grains have the highest LREE contents among the studied apatite, which could provide the LREE for the allanite (Fig. 8B). The limestone wallrocks in the Jinling deposit can also supply abundant Ca.

Fluid metasomatism can significantly influence the ore grades (Broom-Fendley et al., 2016; Broom-Fendley et al., 2017; Hastie et al., 2020; Ying et al., 2020; Petrella et al., 2021). The Fe grades of massive magnetite ores are generally higher in the Jinling deposit (average grade of ~ 52% Fe) than in the Zhangjiawa deposit (average grade of ~ 46% Fe). Fluid metasomatism occurred at the Ap2 stage in the Jinling deposit, prior to the large-scale deposition of Fe (massive magnetite ores). In this stage, besides the apatite, other minerals such as garnet, pyroxene and magnetite (minor) also show porous textures (Fig. 4D, E), indicating that significant leaching of elements (e.g., Fe) occurred. The Ap2b apatite grains have elevated Eu/Eu* and low Ce/Ce* values similar to those of the Ap1 (Fig. 10A). In combination with their high F contents and F/Cl ratios close to the Ap1 (Fig. 7B), the fluids responsible for the metasomatism were probably derived from the similar magmatic fluids of the Ap1. Because F can promote the release of Fe, the metasomatism might leach additional Fe from the Ap2 stage and thus contribute to the formation of high-grade iron ores in the Ap3 stage. In the Zhangjiawa deposit, the metasomatism occurred at the Ap-3 stage. The porous textures in the apatite and magnetite indicate the loss of elements, especially the Fe (Fig. 4G). The metasomatism thus contributed to lower the Fe grade of the magnetite ores. The Ap-3a and Ap-3b apatite do not show significant difference in Eu/Eu* and Ce/Ce* values (Fig. 10A) and F

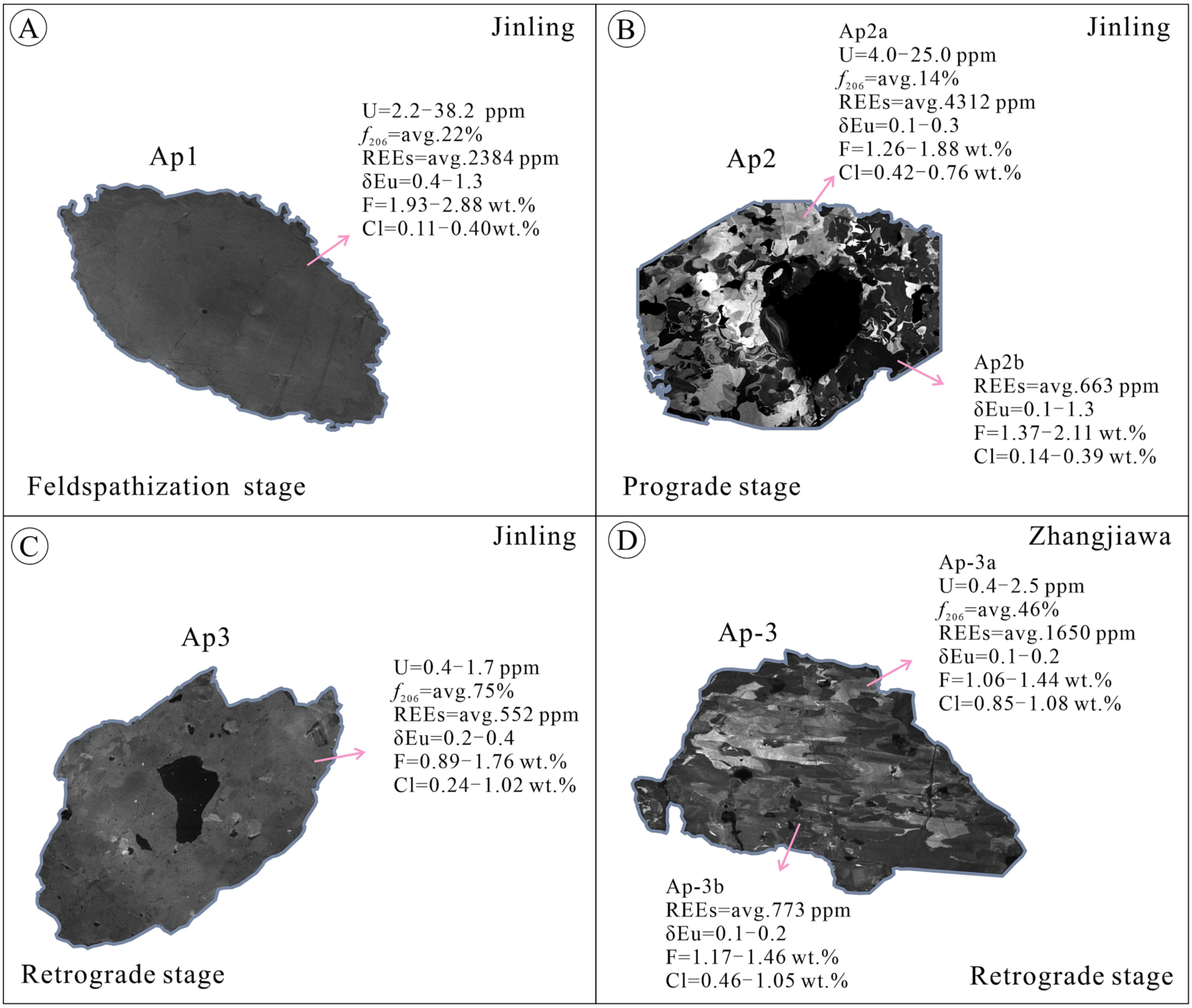

Fig. 13. Summary diagram illustrating the textural and elemental features of different stages of apatite from the Jinling and Zhangjiawa iron deposits.

contents, but the Cl contents decrease more or less from the Ap-3a to the Ap-3b (Fig. 7B). This indicates that low-salinity fluids such as recycling meteoric water might be responsible for the metasomatism.

In summary, fluid metasomatism contributed to the Fe grade. Fluid metasomatism in the Jinling deposit occurred before the massive Fe precipitation, leaching additional Fe from the skarn rocks and thus promoting the formation of high-grade iron ores. In the Zhangjiawa deposit, fluid metasomatism occurred after the massive Fe precipitation, leading to the loss of Fe and thus lowering the Fe grade.

7. Conclusions

In-situ texture, geochronology and geochemistry of apatite from the Jinling and Zhangjiawa Fe skarn deposits were conducted to decipher the ore-forming processes and formation of high-grade iron ores (Fig. 13), leading to the following major conclusions:

(1) The U-Pb ages of primary apatite in the Jinling and Zhangjiawa deposits are 128.3–130.4 Ma and 128.1 ± 4.2 Ma, respectively, which are consistent with the intrusive ages of the spatially associated high-Mg diorites. Combined with the skarn-type mineralization, it corroborates that the ore-forming materials were derived from these rocks.
(2) The apatite grains in the early hydrothermal stage show elevated F contents and F/Cl ratios, indicating the high-F properties of the originally exsolved fluids. The high F contents probably contributed to promote the Fe leaching from the wallrocks.
(3) Based on the Eu/Eu* and Ce/Ce* ratios and S contents in apatite, the oxygen fugacities of the ore-forming fluids increased from the early to the late hydrothermal stages, resulting in the massive deposition of magnetite. The increase of oxygen fugacity was mainly induced by the fluid-rock interaction.
(4) Fluid metasomatism occurred in both the Jinling and Zhangjiawa deposits, which contributed to elevate and lower the Fe grade, respectively. Metasomatism of by high-F fluids before the massive Fe precipitation facilitated the formation of high-grade ores.

Declaration of Competing Interest

The authors declare that they have no known competing financial interests or personal relationships that could have appeared to influence the work reported in this paper.

Data availability

Data will be made available on request.

Acknowledgements

We are grateful to Wenqin Zheng and Xiang Li for EPMA analysis, Shaohua Dong for SEM analysis, and Junjie Han for LA-ICP-MS analysis. We thank Xiaochun Li, Jianfeng Gao, and Jingjing Zhu for advice during the discussion. Anonymous reviewers are also thanked for their constructive and valuable comments. This study is financially supported by the Natural Science Foundation of China (41930430) and the West Light Foundation of The Chinese Academy of Sciences (Grant No. xbzg-zdsys-202108).

Appendix A. Supplementary data

Supplementary data to this article can be found online at https://doi.org/10.1016/j.oregeorev.2023.105483.

References

Alex, A., Zajacz, Z., 2022. The solubility of Cu, Ag and Au in magmatic sulfur bearing fluids as a function of oxygen fugacity. Geochim. Cosmochim. Acta 330, 93–115.

Andersson, S.S., Wagner, T., Jonsson, E., Fusswinkel, T., Whitehouse, M.J., 2019. Apatite as a tracer of the source, chemistry and evolution of ore-forming fluids: the case of the Olserum-Djupedal REE-phosphate mineralisation, SE Sweden. Geochim. Cosmochim. Acta 255, 163–187.

Bell, A.S., Simon, A., 2011. Experimental evidence for the alteration of the Fe^{3+}/ΣFe of silicate melt caused by the degassing of chlorine-bearing aqueous volatiles. Geology 39, 499–502.

Belousova, E.A., Griffin, W.L., O'Reilly, S.Y., Fisher, N.I., 2002. Apatite as an indicator mineral for mineral exploration: trace-element compositions and their relationship to host rock type. J. Geochem. Explor. 76 (1), 45–69.

Bouzari, F., Hart, C.J.R., Bissig, T., Barker, S., 2016. Hydrothermal alteration revealed by apatite luminescence and chemistry: a potential indicator mineral for exploring covered porphyry copper deposits. Econ. Geol. 111 (6), 1397–1410.

Broom-Fendley, S., Styles, M.T., Appleton, J.D., Gunn, G., Wall, F., 2016. Evidence for dissolution-reprecipitation of apatite and preferential LREE mobility in carbonatite-derived late-stage hydrothermal processes. Am. Mineral. 101 (3), 596–611.

Broom-Fendley, S., Brady, A.E., Wall, F., Gunn, G., Dawes, W., 2017. REE minerals at the Songwe Hill carbonatite, Malawi: HREE-enrichment in late-stage apatite. Ore Geol. Rev. 81, 23–41.

Budzyn, B., Harlov, D.E., Williams, M.L., Jercinovic, M.J., 2011. Experimental determination of stability relations between monazite, fluorapatite, allanite, and REE-epidote as a function of pressure, temperature, and fluid composition. Am. Mineral. 96 (10), 1547–1567.

Cao, M.J., Li, G.M., Qin, K.Z., Seitmuratova, E.Y., Liu, Y.S., 2012. Major and trace element characteristics of apatites in granitoids from Central Kazakhstan: Implications for petrogenesis and mineralization. Resour. Geol. 62, 63–83.

Chakhmouradian, A.R., Reguir, E.P., Zaitsev, A.N., Couëslan, C., Xu, C., Kynický, J., Mumin, A.H., Yang, P., 2017. Apatite in carbonatitic rocks: compositional variation, zoning, element partitioning and petrogenetic significance. Lithos 274–275, 188–213.

Chang, Z., Meinert, L.D., 2008. The Empire Cu-Zn mine, Idaho: Exploration implications of unusual skarn features related to high fluorine activity. Econ. Geol. 103 (5), 909–938.

Chelle-Michou, C., Rottier, B., Caricchi, L., Simpson, G., 2017. Tempo of magma degassing and the genesis of porphyry copper deposits. Sci. Rep. 7, 40566.

Chen, Y.-H., Hu, R.-Z., Lan, T.-G., Wang, H., Tang, Y.-W., Yang, Y.-H., Tian, Z.-D., Ulrich, T., 2021. Precise U-Pb dating of grandite garnets by LA-ICP-MS: Assessing ablation behaviors under matrix-matched and non-matrix-matched conditions and applications to various skarn deposits. Chem. Geol. 572, 120198.

Chen, Y.H., Lan, T.G., Wang, H., Tang, Y.W., Dai, Z.H., 2018. LA-ICP-MS trace element characteristics of magnetite from the Zhangjiawa iron deposit, Laiwu and constraints on metallogenic processes. Earth Sci. Front. 25, 032–049 in Chinese with English abstract.

Chen, L., Zheng, T., Xu, W., 2006. A thinned lithospheric image of the Tanlu Fault Zone, eastern China: Constructed from wave equation based receiver function migration. J. Geophys. Res.-Solid Earth 111, B09312.

Cherry, A.R., Kamenetsky, V.S., McPhie, J., Thompson, J.M., Ehrig, K., Meffre, S., Kamenetsky, M.B., Krneta, S., 2018. Tectonothermal events in the Olympic IOCG province constrained by apatite and REE-phosphate geochronology. Aust. J. Earth Sci. 65 (5), 643–659.

Chew, D.M., Petrus, J.A., Kamber, B.S., 2014. U-Pb LA-ICPMS dating using accessory mineral standards with variable common Pb. Chem. Geol. 363, 185–199.

Duan, Z., 2019. The mineralization and mechanism of the iron skarn deposit in Laiwu district, Shandong Province. China University of Geosciences. Ph.D. thesis.(Wuhan) (in Chinese with English abstracts.

Duan, Z., Li, J.W., 2017. Zircon and titanite U-Pb dating of the Zhangjiawa iron skarn deposit, Luxi district, North China Craton: Implications for a craton-wide iron skarn mineralization. Ore Geol. Rev. 89, 309–323.

Fietzke, J., Frische, M., 2016. Experimental evaluation of elemental behavior during LA-ICP-MS: influences of plasma conditions and limits of plasma robustness. J. Anal. At. Spectrom 31 (1), 234–244.

Gammons, C.H., Allin, N.C., 2022. Stability of aqueous Fe(III) chloride complexes and the solubility of hematite between 150 and 300 °C. Geochim. Cosmochim. Acta 330, 148–164.

Gregory, C.J., Rubatto, D., Allen, C.M., Williams, I.S., Hermann, J., Ireland, T., 2007. Allanite micro-geochronology: A LA-ICP-MS and SHRIMP U-Th-Pb study. Chem. Geol. 245 (3-4), 162–182.

Harlov, D.E., Förster, H.J., Nijland, T.G., 2002. Fluid-induced nucleation of REE-phosphate minerals in apatite: nature and experiment. Part I. Chlorapatite. Am. Mineral. 87, 245–261.

Harlov, D.E., Förster, H.J., 2003. Fluid-induced nucleation of REE phosphate minerals in apatite: nature and experiment. Part II. Fluorapatite. American Mineralogist 88, 1209–1229.

Harlov, D.E., Wirth, R., Förster, H.-J., 2005. An experimental study of dissolution-reprecipitation in fluorapatite: fluid infiltration and the formation of monazite. Contrib. Miner. Petrol. 150 (3), 268–286.

Harlov, D.E., Meighan, C.J., Kerr, I.D., Samson, I.M., 2016. Mineralogy, chemistry, and fluid-aided evolution of the pea ridge Fe oxide-(Y+REE) deposit, Southeast Missouri, USA. Econ. Geol. 111 (8), 1963–1984.

Hastie, E.C.G., Kontak, D.J., Lafrance, B., 2020. Gold Remobilization: Insights from Gold Deposits in the Archean Swayze Greenstone Belt, Abitibi Subprovince, Canada. Econ. Geol. 115, 241–277.

Heinrich, C.A., Günther, D., Audétat, A., Ulrich, T., Frischknecht, R., 1999. Metal fractionation between magmatic brine and vapor, determined by microanalysis of fluid inclusions. Geology 27, 755–758.

Henning, P.A., Adolfsson, E., Grins, J., 2000. The chalcogenide phosphate apatites Ca$_{10}$(PO$_4$)$_6$S, Sr$_{10}$(PO$_4$)$_6$S, Ba$_{10}$(PO$_4$)$_6$S and Ca$_{10}$(PO$_4$)$_6$Se. Zeitschriftfür Kristallographie-Crystalline Materials 215, 105110.

Holloway, J.R., 1976. Fluids in the evolution of granitic magmas: consequences of finite CO$_2$ solubility. Geol. Soc. Am. Bull. 87, 1513–1518.

Hu, H., Li, J., Lentz, D., Ren, Z., Zhao, X., Deng, X., Hall, D., 2014. Dissolution-reprecipitation process of magnetite from the Chengchao iron deposit: Insights into ore genesis and implication for in-situ chemical analysis of magnetite. Ore Geol. Rev. 57, 393–405.

Hu, L., Li, Y.K., Wu, Z.J., Bai, Y., W, a.j.,, 2019. Two metasomatic events recorded in apatite from the ore-hosting dolomite marble and implications for genesis of the giant Bayan Obo REE deposit, Inner Mongolia, Northern China. J. Asian Earth Sci. 172, 56–65.

Jin, Z.L., Zhang, Z.C., Hou, T., Santosh, M., Han, L., 2015. Genetic relationship of high-Mg dioritic pluton to iron mineralization: A case study from the Jinling skarn-type iron deposit in the North China Craton. J. Asian Earth Sci. 113, 957–979.

Konecke, B.A., Fiege, A., Simon, A.C., Parat, F., Stechern, A., 2017. Co-variability of S^{6+}, S^{4+}, and S^{2-} in apatite as a function of oxidation state: implications for a new oxybarometer. Am. Mineral. 102 (3), 548–557.

Krneta, S., Cook, N.J., Ciobanu, C.L., Ehrig, K., Kontonikas-Charos, A., 2017. The wirrda well and acropolis prospects, gawler craton, south Australia: insights into evolving fluid conditions through apatite chemistry. J. Geochem. Explor. 181, 276–291.

Lan, T.G., Hu, R.Z., Chen, Y.H., Wang, H., Tang, Y.W., Liu, L., 2019. Generation of high-Mg diorites and associated iron mineralization within an intracontinental setting: Insights from ore-barren and ore-bearing intrusions in the eastern North China Craton. Gondw. Res. 72, 97–119.

Li, S.R., Santosh, M., 2014. Metallogeny and craton destruction: Records from the North China Craton. Ore Geol. Rev. 56, 376–414.

Li, W., Xie, G., Mao, J., Zhu, Q., Zheng, J., 2019. Mineralogy, fluid inclusion, and stable isotope studies of the Chengchao deposit, Hubei Province, Eastern China: Implications for the formation of high-grade Fe skarn deposits. Econ. Geol. 114, 325–352.

Li, X.C., Zhou, M.F., 2015. Multiple stages of hydrothermal REE remobilization recorded in fluorapatite in the paleoproterozoic Yinachang Fe–Cu–(REE) deposit, Southwest China. Geochim. Cosmochim. Acta 166, 53–73.

Liao, W., Su, Z.-K., Li, X.-C., Zhang, C., Zhao, X.-F., 2022. Cathodoluminescent, chemical and strontium isotopic characteristics of apatite from Lanniping Fe-Cu deposit, southwestern China: Implications for fluid evolution in IOCG systems. Ore Geol. Rev. 145, 104882.

Liu, Y., Hu, Z., Gao, S., Günther, D., Xu, J., Gao, C., Chen, H., 2008. In situ analysis of major and trace elements of anhydrous minerals by LA-ICP-MS without applying an internal standard. Chem. Geol. 257 (1-2), 34–43.

Lu, S., Zhao, G., Wang, H., Hao, G., 2008. Precambrian metamorphic basement and sedimentary cover of the North China Craton: A review. Precambr. Res. 160 (1-2), 77–93.

Ludwig, K.R., 2003. User's Manual for Isoplot 3.00, a Geochronological Toolkit for Microsoft Excel. Berkeley Geochronological Center Special Publication 4, 25–32.

Mao, J., Pirajno, F., Cook, N., 2011. Mesozoic metallogeny in East-China and corresponding geodynamic settings-an introduction to the special issue. Ore Geol. Rev. 43 (1), 1–7.

Mao, M., Rukhlov, A.S., Rowins, S.M., Spence, J., Coogan, L.A., 2016. Apatite trace element compositions: a robust new tool for mineral exploration. Econ. Geol. 111 (5), 1187–1222.

McPhie, J., Kamenetsky, V., Allen, S., Ehrig, K., Agangi, A., Bath, A., 2011. The fluorine link between a supergiant ore deposit and a silicic large igneous province. Geology 39, 1003–1006.

Meinert, L.D., Hefton, K.K., Mayes, D., Tasiran, I., 1997. Geology, zonation, and fluid evolution of the Big Gossan Cu-Au skarn deposit, Ertsberg District, Irian Jaya. Econ. Geol. 92, 509–534.

Meinert, L.D., Dipple, G.M., Nicolescu, S., 2005. World skarn deposits. Econ. Geol. 100, 299–336.

Mercer, C.N., Watts, K.E., Gross, J., 2020. Apatite trace element geochemistry and cathodoluminescent textures—A comparison between regional Magmatism and the Pea Ridge IOAREE and Boss IOCG deposits, southeastern Missouri iron metallogenic province, USA. Ore Geol. Rev. 116, 103–129.

Migdisov, A.A., Williams-Jones, A.E., 2014. Hydrothermal transport and deposition of the rare earth elements by fluorine-bearing aqueous liquids. Miner. Deposita 49 (8), 987–997.

Palma, G., Barra, F., Reich, M., Valencia, V., Simon, A.C., Vervoort, J., Leisen, M., Romero, R., 2019. Halogens, trace element concentrations, and Sr-Nd isotopes in apatite from iron oxide-apatite (IOA) deposits in the Chilean iron belt: evidence for magmatic and hydrothermal stages of mineralization. Geochim. Cosmochim. Acta 246, 515–540.

Pan, Y., Fleet, M.E., 2002. Composition of the apatite-group minerals: substitution mechanisms and controlling factors. Rev. Mineral. Geochem. 48, 13–49.

Pan, L.C., Hu, R.Z., Wang, X.S., Bi, X.W., Zhu, J.J., Li, C.S., 2016. Apatite trace element and halogen compositions as petrogenetic-metallogenic indicators: examples from four granite plutons in the Sanjiang region, SW China. Lithos 254–255, 118–130.

Park, C., Park, C., Song, Y., Choi, S.-G., 2019. Sequential trace element analysis of zoned skarn garnet: implications for multi-stage fluxing and flow of magmatic fluid into a skarn system. Lithos 350-351, 105213.

Petrella, L., Thébaud, N., Evans, K., LaFlamme, C., Occhipinti, S., 2021. The role of competitive fluid-rock interaction processes in the formation of high-grade gold deposits. Geochim. Cosmochim. Acta 313, 38–54.

Piccoli, P.M., Candela, P.A., 2002. Apatite in Igneous Systems. In Phosphates: geochemical, geobiological, and materials importance (Eds. M.J. Kohn, Rakovan, J. M. Hughes). Rev. Mineral. Geochem. 48 (1), 255–292.

Qiu, J.S., Loh, C.H., McInnes, B.I.A., Zhou, J.C., 2000. Potash-rich magmatism and associated gold-copper mineralization in the Yishu deep fault zone and its vicinity, eastern China. Resour. Geol. 50, 269–280.

Ren, J., Tamaki, K., Li, S., Junxia, Z., 2002. Late Mesozoic and Cenozoic rifting and its dynamic setting in Eastern China and adjacent areas. Tectonophysics 344 (3-4), 175–205.

Roy-Garand, A., Adlakha, E., Hanley, J., Elongo, V., Lecumberri-Sanchez, P., Falck, H., Boucher, B., 2022. Timing and sources of skarn mineralization in the Canadian Tungsten Belt: revisiting the paragenesis, crystal chemistry and geochronology of apatite. Miner. Deposita 57 (8), 1391–1413.

Seo, J.H., Guillong, M., Heinrich, C.A., 2009. The role of sulfur in the formation of magmatic-hydrothermal copper-gold deposits. Earth Planet. Sci. Lett. 282 (1-4), 323–328.

Seward, T.M., Barnes, H.L., 1997. Metal transport by hydrothermal ore fluids. In: Barnes, H.L. (Ed.), Geochemistry of hydrothermal ore deposits. John Wiley and Sons, New York, pp. 435–486.

Sha, L.-K., Chappell, B.W., 1999. Apatite chemical composition, determined by electron microprobe and laser-ablation inductively coupled plasma mass spectrometry, as a probe into granite petrogenesis. Geochim. Cosmochim. Acta 63 (22), 3861–3881.

Shu, Q.H., Chang, Z.H., Hammerli, J., Lai, Y., Huizenga, J.M., 2017. Composition and evolution of fluids forming the Baiyinnuo'er Zn-Pb skarn deposit, northeastern China: Insights from laser ablation ICP-MS study of fluid inclusions. Econ. Geol. 112, 1441–1460.

Simon, A.C., Pettke, T., Candela, P.A., Piccoli, P.M., Heinrich, C.A., 2004. Magnetite solubility and iron transport in magmatic-hydrothermal environments. Geochim. Cosmochim. Acta 68 (23), 4905–4914.

Simon, A.C., Ripley, E.M., 2011. The role of magmatic sulfur in the formation of ore deposits. Rev. Mineral. Geochem. 73 (1), 513–578.

Song, W.L., Xu, C., Smith, M.P., Chakhmouradian, A.R., Brenna, M., Kynický, J., Chen, W., Yang, Y.H., Deng, M., Tang, H.Y., 2018. Genesis of the world's largest rare earth element deposit, Bayan Obo, China: protracted mineralization evolution over ~1 b.y. Geology 46, 323–326.

Tera, F., Wasserburg, G.J., 1972. U-Th-Pb systematics in three Apollo 14 basalts and the problem of initial Pb in lunar rocks. Earth Planet. Sci. Lett. 14 (3), 281–304.

Thompson, J., Meffre, S., Maas, R., Kamenetsky, V., Kamenetsky, M., Goemann, K., Ehrig, K., Danyushevsky, L., 2016. Matrix effects in Pb/U measurements during LA-ICP-MS analysis of the mineral apatite. J. Anal. At. Spectrom 31 (6), 1206–1215.

Thomson, S.N., Gehrels, G.E., Ruiz, J., Buchwaldt, R., 2012. Routine low-damage apatite U-Pb dating using laser ablation-multicollector-ICPMS. Geochemistry Geophysics Geosystems 13, 1–23.

Wen, G., Bi, S.-J., Li, J.-W., 2017. Role of evaporitic sulfates in iron skarn mineralization: a fluid inclusion and sulfur isotope study from the Xishimen deposit, Handan-Xingtai district, North China Craton. Miner. Deposita 52 (4), 495–514.

Williams-Jones, A.E., Heinrich, C.A., 2005. Vapor transport of metals and the formation of magmatic–hydrothermal ore deposits: 100th anniversary special paper. Econ. Geol. 100, 1287–1312.

Williams-Jones, A.E., Migdisov, A.A., 2014. Experimental Constraints on the Transport and Deposition of Metals in Ore-Forming Hydrothermal Systems. In: Kelley, K.D., Golden, H.C. (Eds.), Building Exploration Capability for the 21st Century. Society of Economic Geologists.

Williams-Jones, A.E., Samson, I.M., Ault, K.M., Gagnon, J.E., Fryer, B.J., 2010. The genesis of distal zinc skarns: Evidence from the Mochito deposit, Honduras. Econ. Geol. 105 (8), 1411–1440.

Wood, S.A., Samson, I.M., 1998. Solubility of ore minerals and complexation of ore metals in hydrothermal solutions. Rev. Econ. Geol. 10, 33–80.

Xiao, B., Pan, Y., Song, H., Song, W., Zhang, Y.u., Chen, H., 2021. Hydrothermal alteration processes of fluorapatite and implications for REE remobilization and mineralization. Contrib. Miner. Petrol. 176 (10).

Xing, Y.L., Etschmann, B., Liu, W.H., Mei, Y., Shvarov, Y., Testemale, D., Tomkins, A., Brugger, J., 2019. The role of fluorine in hydrothermal mobilization and transportation of Fe, U and REE and the formation of IOCG deposits. Chem. Geol. 504, 158–176.

Xing, K., Shu, Q.H., Lentz, D.R., 2021. Constraints on the formation of the giant Daheishan porphyry Mo deposit (NE China) from whole-rock and accessory mineral geochemistry. J. Petrol. 62, egab018.

Yang, D.B., Yang, H.T., Shi, J.P., Xu, W.L., Wang, F., 2017. Sedimentary response to the paleogeographic and tectonic evolution of the southern North China Craton during the late Paleozoic and Mesozoic. Gondw. Res. 49, 278–295.

Yardley, B.W., 2005. Metal concentrations in crustal fluids and their relationship to ore formation. Econ. Geol. 100, 613–632.

Ying, Y.C., Chen, W., Simonetti, A., Jiang, S.Y., Zhao, K.D., 2020. Significance of hydrothermal reworking for REE mineralization associated with carbonatite: constraints from in situ trace element and C-Sr isotope study of calcite and apatite from the Miaoya carbonatite complex (China). Geochim. Cosmochim. Acta 280, 340–359.

Zeng, L.-P., Zhao, X.-F., Li, X.-C., Hu, H., McFarlane, C., 2016. In situ elemental and isotopic analysis of fluorapatite from the Taocun magnetite-apatite deposit, Eastern China: constraints on fluid metasomatism. Am. Mineral. 101 (11), 2468–2483.

Zhai, M.-G., Santosh, M., 2011. The early Precambrian odyssey of the North China Craton: A synoptic overview. Gondw. Res. 20 (1), 6–25.

Zhang, Y.M., Gu, X.X., Liu, L., Dong, S.Y., Li, K., Li, B.H., Lv, P.R., 2011. Fluid inclusion and H-O isotope evidence for immiscibility during mineralization of the Yinan Au-Cu-Fe deposit, Shandong, China. J. Asian Earth Sci. 42 (1-2), 83–96.

Zhang, Z., Li, H., Li, J., Song, X.-Y., Hu, H., Li, L., Chai, F., Hou, T., Xu, D., 2021. Geological settings and metallogenesis of high-grade iron deposits in China. Sci. China Earth Sci. 64 (5), 691–715.

Zhao, G.C., Cawood, P.A., Li, S.Z., Wilde, S.A., Sun, M., Zhang, J., He, Y.H., Yin, C.Q., 2012. Amalgamation of the North China Craton: Key issues and discussion. Precambr. Res. 222–223, 55–76.

Zhou, R.J., Wen, G., Li, J.W., Jiang, S.Y., Hu, H., Deng, X.D., Zhao, X.F., Yan, D.R., Wei, K.T., Cai, H.A., Shang, S.C., Li, B.C., Dai, X.K., 2022. Apatite chemistry as a petrogenetic–metallogenic indicator for skarn ore-related granitoids: an example from the Daye Fe-Cu-(Au-Mo-W) district, Eastern China. Contrib. Miner. Petrol. 177, 23.

Zhu, RiXiang, Xu, YiGang, Zhu, G., Zhang, HongFu, Xia, QunKe, Zheng, TianYu, 2012. Destruction of the North China Craton. Sci. China Earth Sci. 55 (10), 1565–1587.